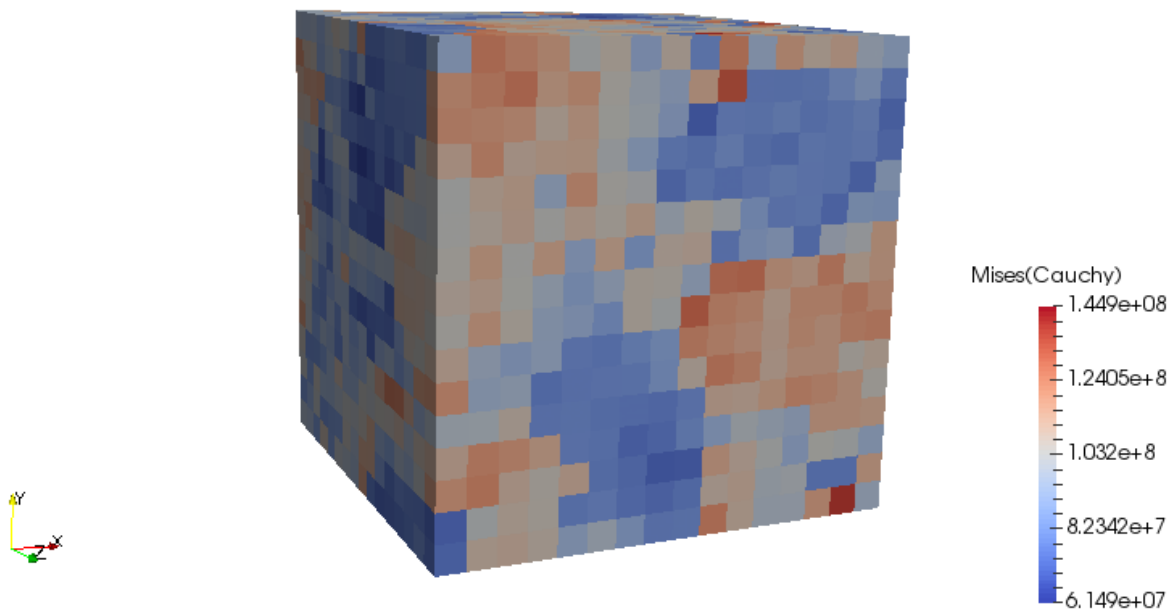


Master thesis Nr. 16-148

Modeling of hardening behavior for steel and aluminium based on extended crystal plasticity model

Hui Zhou



Adviser: Bekim Berisha, Christian Raemy

Institute of Virtual Manufacturing
Prof. Dr. Pavel Hora
ETH Zurich

03.10.2016

ETH Zurich
Institute of Virtual Manufacturing
CLA F 07.0
Tannenstrasse 3
8092 Zurich

Telefon: +41 (0)44 632 26 10
Fax: +41 (0)44 632 11 65

sek@ivp.mavt.ethz.ch
www.ivp.ethz.ch

Confirmation of originality

(DEUTSCH/ENGLISCH bitte nicht verwendete Version löschen)

I hereby confirm that I am the sole author of the written work here enclosed and that I have compiled it in my own words. Parts excepted are corrections of form and content by the supervisor. With my signature I confirm that

- I have committed none of the forms of plagiarism described in the - Citation etiquette - information sheet.
- I have documented all methods, data and processes truthfully.
- I have not manipulated any data.
- I have mentioned all persons who were significant facilitators of the work.
- I am aware that the work may be screened electronically for plagiarism.

Place, date:

Signature(s):

Abstract

Material parameter calibration is an essential step for crystal plasticity simulation. Unlike macroscopic flow curve fitting, it requires virtual test to express the stress-strain relationship in the macroscopic level. In this paper, plastic phenomenological model is used for virtual test of the representative volume element (RVE). The virtual test is executed by the spectral solver of DAMASK software. To obtain the optimal parameters, Trust-Region-Reflective least squares fitting is used to minimize the error between simulation data and experimental data. An approach for the initial parameter guess is proposed since a good initial guess decreases the simulation times. The approach is practiced by the uniaxial tension-compression test of steel and simple shear-reverse shear test of aluminium. Besides, the homogeneous anisotropic hardening(HAH) model is fit by the virtual test.

1 Introduction

Modeling the strain-stress behavior of metal material is always a key task for the study of plasticity. Due to the advancement of observation technique, material can be viewed from macroscopic scale, mesoscopic scale to atomistic scale. Depending on the size of object we want to simulate, different theories and methods are applicable for different length scales as shown in Table(1). Generally, the length scale for engineering simulation is up to mesoscopic scale. To link dislocation dynamics and continuum mechanics, crystal plasticity is proposed.

scale	atomistic	mesoscopic	macroscopic
theory	quantum mechanics	statistical mechanics	continuum mechanics
method(e.g.)	Molecular Dynamics	Dislocation Dynamics	Finite Element

Table 1: Theories and simulation methods for different length scales

It assumes that the cause of plasticity is due to dislocation. The corresponding crystal plasticity finite element method (CPFEM) exhibits the material anisotropy. It takes a integration point of an element as a representative volume element (RVE) composed of different grains. Each grain distinguishes between each other by its constituents. The constituent is distinguished by its phase, texture and volume fraction. DAMASK software is designed according to this idea. In this chapter, some preliminary concepts from continuum mechanics will be given to facilitate reading the next chapter.

1.1 Finite strain theory

Consider a continuum body $\mathcal{B} \subset \mathcal{R}^3$ in the Cartesian coordinates, the deformation field $\chi_{t_0}^t : \mathbf{X} = \mathbf{x}(t_0) \in \mathcal{B}^{t_0} \rightarrow \mathbf{x} \in \mathcal{B}^t$ maps the reference configuration (Lagrangian coordinates) to the current configuration (Eulerian coordinates) and the deformation gradient $\mathbf{F}_{t_0}^t$ is defined by

$$\mathbf{F}_{t_0}^t = \nabla \chi_{t_0}^t = \frac{d\mathbf{x}}{d\mathbf{X}} \quad (1.1)$$

which is smooth and preserves the orientation $\det(\mathbf{F}_{t_0}^t) > 0$. Following the common notation of deformation gradient, $\mathbf{F}_{t_0}^t$ is simplified as \mathbf{F} . According to the principle of linear momentum, the equilibrium equation without body force in the current configuration is

$$\text{div}(\boldsymbol{\sigma}) = 0, \mathbf{x} \in \mathcal{B} \quad (1.2a)$$

$$\boldsymbol{\sigma} \cdot \mathbf{n} = \mathbf{t}, \mathbf{x} \in \partial\mathcal{B}_\sigma \quad (1.2b)$$

$$\mathbf{u} = \mathbf{u}_0, \mathbf{x} \in \partial\mathcal{B}_u \quad (1.2c)$$

where $\boldsymbol{\sigma}$ is Cauchy stress, \mathbf{u} is displacement, \mathbf{t} and \mathbf{u}_0 are force and displacement boundary conditions. The boundary conditions are complementary (i.e., $\partial\mathcal{B}_\sigma \cup \partial\mathcal{B}_u = \partial\mathcal{B}, \partial\mathcal{B}_\sigma \cap \partial\mathcal{B}_u = \emptyset$). In the reference configuration, the equilibrium equation without body force is

$$\text{Div}(\mathbf{P}) = 0, \mathbf{X} \in \mathcal{B}^{t_0} \quad (1.3a)$$

$$\mathbf{P} = \mathbf{P}_{BC}, \mathbf{X} \in \partial\mathcal{B}_P^{t_0} \quad (1.3b)$$

$$\mathbf{F} = \mathbf{F}_{BC}, \mathbf{X} \in \partial\mathcal{B}_F^{t_0} \quad (1.3c)$$

where \mathbf{P} is first Piola-Kirchhoff stress and \mathbf{P}_{BC} , \mathbf{F}_{BC} are boundary conditions. The boundary conditions are also complementary. In addition, the principle of angular momentum requires Cauchy stress $\boldsymbol{\sigma}$ and second Piola-Kirchhoff stress \mathbf{S} to be symmetric. The stress and strain in different configurations fulfill the work conjugate,

$$\boldsymbol{\sigma} : \dot{\boldsymbol{\epsilon}} = \mathbf{P} : \dot{\mathbf{F}} = \mathbf{S} : \dot{\mathbf{E}} = \sigma_e : \dot{\epsilon}^p \quad (1.4)$$

where infinitesimal strain tensor $\boldsymbol{\epsilon} = \frac{1}{2}(\nabla \mathbf{u} + \mathbf{u} \nabla)$, Green-Lagrangian strain tensor $\mathbf{E} = \frac{1}{2}(\mathbf{F}^T \cdot \mathbf{F} - \mathbf{I})$, equivalent stress $\sigma_e = \sqrt{\frac{3}{2} \boldsymbol{\sigma} : \boldsymbol{\sigma}}$ and equivalent plastic strain rate $\dot{\epsilon}^p = \sqrt{\frac{2}{3} \dot{\epsilon}^p : \dot{\epsilon}^p}$ according to von Mises' rule. For uniaxial test, $\sigma_e = |\sigma_{11}|$ and $\epsilon^p = |\epsilon_{11}^p|$. For simple shear test, $\sigma_e = \sqrt{3} |\tau|$ and $\epsilon^p = \frac{|\gamma|}{\sqrt{3}}$, where τ and γ is shear stress and strain.

1.2 Linear elasticity

In the range of linear elasticity, the constitutive law $\boldsymbol{\sigma}(\boldsymbol{\epsilon})$ is the Hooke's law. Namely,

$$\boldsymbol{\sigma} = \mathbf{C} : \boldsymbol{\epsilon} \quad (1.5)$$

where stiffness tensor \mathbf{C} in the symmetric Voigt form is

$$\mathbf{C} = \begin{pmatrix} c_{11} & c_{12} & c_{13} & c_{14} & c_{15} & c_{16} \\ & c_{22} & c_{23} & c_{24} & c_{25} & c_{26} \\ & & c_{33} & c_{34} & c_{35} & c_{36} \\ & & & c_{44} & c_{45} & c_{46} \\ & & & & c_{55} & c_{56} \\ & & & & & c_{66} \end{pmatrix} \quad (1.6)$$

For the orthotropic material, stiffness tensor \mathbf{C} becomes

$$\mathbf{C} = \begin{pmatrix} c_{11} & c_{12} & c_{13} & 0 & 0 & 0 \\ & c_{22} & c_{23} & 0 & 0 & 0 \\ & & c_{33} & 0 & 0 & 0 \\ & & & c_{44} & 0 & 0 \\ & & & & c_{55} & 0 \\ & & & & & c_{66} \end{pmatrix} \quad (1.7)$$

Furthermore, material with face centered cubic (fcc) or body centered cubic (bcc) lattice structure is transverse isotropic. So stiffness tensor \mathbf{C} is composed of 3 independent elastic constants $c_{11} = c_{22} = c_{33}$, $c_{12} = c_{23} = c_{13}$, $c_{44} = c_{55} = c_{66}$. If the boundary conditions and the distribution of stiffness tensor are known, then the equilibrium equation Eq.(1.2) combined with the Hooke's law Eq.(1.5) can be solved using finite element method. The solution $\boldsymbol{\sigma}$ can be expressed analytically $\boldsymbol{\sigma} = \nabla \times \nabla \times \Phi$, where Φ is the stress function [31]. This is a forward problem. From the distribution of stiffness tensor and boundary conditions, the stress and strain distribution are obtained. Conversely, if the force and displacement distribution at the boundary $\partial\mathcal{B}$ are known but the distribution of stiffness tensor is unknown, this is an inverse problem. Usually, the method to solve inverse problem is numerical optimization [20]. The

inverse problem is much more difficult than the forward problem because it is ill posed. For instance, from Hooke's law Eq.(1.5), it is easy to obtain stress σ if stiffness tensor C and strain ϵ are known. However, it is difficult to obtain stiffness tensor C if stress σ and strain ϵ are known.

1.3 Crystal plasticity

As for plasticity, the constitutive law $P = P(F)$ gives the incremental relationship: $dP = \frac{dP}{dF} : dF = C : dF$, $dF = \frac{dF}{dP} : dP = S : dP$ where incremental stiffness tensor C and incremental compliance tensor S are determined by the material parameters of plastic model. In detail, the deformation gradient F can be decomposed as elastic part F^e and plastic part F^p [25],

$$F = F^e \cdot F^p \quad (1.8)$$

where F^p represents the history of plastic deformation and F^e includes the rotation. This kind of decomposition is similar to the decomposition of infinitesimal strain,

$$\epsilon = \epsilon^e + \epsilon^p \quad (1.9)$$

The difference is Eq.(1.8) includes the nonlinear mapping but Eq.(1.9) is only linear superposition. Furthermore, the velocity gradient $L = \frac{d\dot{x}}{dx}$ can be written as

$$L = \dot{F} \cdot F^{-1} = \dot{F}^e \cdot (F^e)^{-1} + F^e \cdot \dot{F}^p \cdot F^p \cdot (F^e)^{-1} = L^e + L^p \quad (1.10)$$

In the CPFEM, the plastic velocity gradient L^p is determined by the shear strain rate $\dot{\gamma}^\alpha$ on all active slip systems α ,

$$L^p = \sum_{\alpha=1}^A \dot{\gamma}^\alpha s^\alpha \otimes n^\alpha \quad (1.11)$$

where A is the number of active slip systems, s^α is the slip direction and n^α is the normal of slip plane. Note that the decomposition Eq.(1.8) maps reference configuration to intermediate configuration until current configuration. The corresponding strain and stress are listed in Table(2). From reference configuration to intermediate configuration, the lattice does not

Reference configuration		Intermediate configuration		Current configuration
$(X, s^0 \otimes n^0)$	$\xrightarrow{F^p}$	$(x^*, s \otimes n)$	$\xrightarrow{F^e}$	$(x, s^t \otimes n^t)$
S, E	$\xrightarrow{F^p}$	T^*, E^*	$\xrightarrow{F^e}$	σ, ϵ

Table 2: Decomposition of deformation gradient $F = F_e F_p$

distort (i.e. $s^0 \otimes n^0 = s \otimes n$). The stress and strain for intermediate configuration are related by,

$$T^* = (F^e)^{-1} \cdot \det(F^e) \sigma \cdot (F^e)^{-T} \quad (1.12a)$$

$$E^* = \frac{1}{2} \left[(F^e)^T \cdot F^e - I \right] \quad (1.12b)$$

The application of plastic model yields implicit ordinary differential equations (ODEs) of shear strain rate $\dot{\gamma}^\alpha$ and slip resistance $\dot{\tau}_c^\alpha$ on the slip system α [30],

$$\dot{\gamma}^\alpha = f(\tau^\alpha, \tau_c^\alpha) \quad (1.13a)$$

$$\tau_c^\alpha = g(\gamma, \dot{\gamma}, \kappa) \quad (1.13b)$$

where κ is an internal variable relates geometrically necessary dislocations (i.e. κ can be a function of geometric dislocation tensor G [14], intrinsic material length ℓ and effective strain gradient η_G^α [15]). In particular, the viscoplastic power-law model is used commonly in literature,

$$\tau^\alpha = \tau_c^\alpha |\dot{\gamma}^\alpha|^{\frac{1}{n}} \text{sgn}(\dot{\gamma}^\alpha) \quad (1.14a)$$

$$\dot{\tau}_c^\alpha = \sum_{k=1}^A h^{\alpha k}(\tau_c, \kappa) \left| \dot{\gamma}^k \right| \quad (1.14b)$$

where $n > 0$ is a constant determining the rate sensitivity. $h^{\alpha k}$ is the hardening function. Using numerical integration scheme, Eqs.(1.14) give explicit constitutive relation $\tau(\gamma, \kappa)$.

2 Theory

In this chapter, an overview of DAMASK plastic phenomenological power-law model will be presented first. DAMASK uses crystal plasticity to provide the constitutive law $P(F)$ and spectral method [9] to solve the forward problem Eq.(1.3) on the RVE. For DAMASK spectral solver, the inputs are material parameters, geometry data, load cases and the outputs are stress tensor and strain tensor. DAMASK also provides interfaces for commercial FEM softwares Abaqus and Marc. An approach for material parameter calibration will be given next. Basically, the approach uses DAMASK spectral solver to fit the flow curve from experiment.

2.1 phenomenological power-law model

In DAMASK, the power-law viscoplastic model Eqs.(1.14) gives the shear strain rate $\dot{\gamma}^\alpha$ in terms of the resolved shear stress τ^α ,

$$\dot{\gamma}^\alpha = \dot{\gamma}_{\text{slip}}^0 \left| \frac{\tau^\alpha}{\tau_c^\alpha} \right|^{n_{\text{slip}}} \text{sgn}(\tau^\alpha) \quad (2.1)$$

where $\dot{\gamma}_{\text{slip}}^0$ is the reference shear strain rate, n_{slip} characterizes the rate dependence and the slip resistance τ_c^α follows the hardening law,

$$\dot{\tau}_c^\alpha = \sum_{k=1}^A h^{\alpha k} |\dot{\gamma}^k| \quad (2.2)$$

The interactive hardening function $h^{\alpha k}$ is given by

$$h^{\alpha k} = q^{\alpha k} \left[h^0 \left(1 - \frac{\tau_c^k}{\tau_s} \right)^a \right] \quad (2.3)$$

where h^0, τ_s and a are material parameters for hardening, $q^{\alpha k}$ is 1.0 for coplanar slip systems α, k and 1.4 for others. The resolved shear stress τ^α for bcc material includes non-Schmid effects [19],

$$\begin{aligned} \tau_+^\alpha &= \boldsymbol{\sigma} : \mathbf{s}^\alpha \otimes \mathbf{n}^\alpha + \\ & a_1 \boldsymbol{\sigma} : \mathbf{s}^\alpha \otimes \mathbf{n}_1^\alpha + a_2 \boldsymbol{\sigma} : (\mathbf{n}^\alpha \times \mathbf{s}^\alpha) \otimes \mathbf{n}^\alpha + a_3 \boldsymbol{\sigma} : (\mathbf{n}_1 \times \mathbf{s}^\alpha) \otimes \mathbf{n}_1^\alpha + \\ & a_4 \boldsymbol{\sigma} : \mathbf{n}^\alpha \otimes \mathbf{n}^\alpha + a_5 \boldsymbol{\sigma} : (\mathbf{n}^\alpha \times \mathbf{s}^\alpha) \otimes (\mathbf{n}^\alpha \times \mathbf{s}^\alpha) + a_6 \boldsymbol{\sigma} : \mathbf{s}^\alpha \otimes \mathbf{s}^\alpha \\ & = \boldsymbol{\sigma} : \mathbf{s}^\alpha \otimes \mathbf{n}^\alpha + \boldsymbol{\sigma} : \mathbf{s}_+^\alpha \otimes \mathbf{n}^\alpha \end{aligned} \quad (2.4)$$

where the first term is Schmid's law, \mathbf{n}_1^α is rotated from \mathbf{n}^α by an angle of $\frac{\pi}{3}$ with respect to the axis \mathbf{s}^α and $\mathbf{s}_+^\alpha \otimes \mathbf{n}^\alpha$ represents the non-Schmid tensor at the positive slip direction. Together with negative slip direction $-\mathbf{s}^\alpha$, the non-Schmid tensor has $2 * 6$ terms,

$$\tau^\alpha = \frac{1}{2} (\tau_+^\alpha + \tau_-^\alpha) = \boldsymbol{\sigma} : \mathbf{s}^\alpha \otimes \mathbf{n}^\alpha + \frac{1}{2} (\boldsymbol{\sigma} : \mathbf{s}_+^\alpha \otimes \mathbf{n}^\alpha + \boldsymbol{\sigma} : \mathbf{s}_-^\alpha \otimes \mathbf{n}^\alpha) = \boldsymbol{\sigma} : \mathbf{s}_{\text{slip}}^\alpha \otimes \mathbf{n}_{\text{slip}}^\alpha \quad (2.5)$$

Despite the slip systems, DAMASK extends the plastic velocity gradient \mathbf{L}^p to include the

deformation twinning,

$$\mathbf{L}^p = \left(1 - \sum_{\beta=1}^B f^\beta\right) \sum_{\alpha=1}^A \dot{\gamma}^\alpha \mathbf{s}^\alpha \otimes \mathbf{n}^\alpha + \sum_{\beta=1}^B \gamma_{\text{twin}} \dot{f}^\beta \mathbf{s}_{\text{twin}}^\beta \otimes \mathbf{n}_{\text{twin}}^\beta \quad (2.6)$$

where f is the volume fraction of twinned region for twinning systems β , B is the number of twinning systems and γ_{twin} is the characteristic twin shear (e.g. $\frac{\sqrt{2}}{2}$ for fcc, bcc lattice structures). The evolution of volume fraction uses the similar phenomenological power-law equation,

$$\dot{f}^\beta = \begin{cases} \left(1 - \sum_{\beta=1}^B f^\beta\right) \frac{\dot{\gamma}_{\text{twin}}^0}{\gamma_{\text{twin}}} \left(\frac{\tau^\beta}{\tau_c^\beta}\right)^{n_{\text{twin}}} & \text{if } \tau^\beta > 0 \\ 0 & \text{if } \tau^\beta \leq 0 \end{cases} \quad (2.7)$$

with the constraints $f^\beta \geq 0$ and $\sum_{\beta=1}^B f^\beta \leq 1$. Since the addition of twinning, the evolution of slip resistance τ_c^α Eq.(2.2) is modified as,

$$\dot{\tau}_c^\alpha = h_{ss}^0 \left[1 + C \left(\sum_{\beta=1}^B f^\beta\right)^b\right] \sum_{k=1}^A q_{ss}^{\alpha k} \left(1 - \frac{\tau_k}{\tau_s + s_{pr} \sqrt{\sum_{\beta=1}^B f^\beta}}\right)^a |\dot{\gamma}^k| \quad (2.8)$$

where h_{ss}^0 and $q_{ss}^{\alpha k}$ are hardening parameters for slip-slip interaction, parameters C and b account for Basinski effect, parameter s_{pr} represents the contribution of Hall-Petch effect [32]. The twinning hardening function is given as

$$\dot{\tau}_c^\beta = h_{ts}^0 \left(\sum_{k=1}^A |\dot{\gamma}^k|\right)^e \sum_{k=1}^A q_{ts}^{\beta k} |\dot{\gamma}^k| + h_{tt}^0 \left(\sum_{k=1}^B f^\beta\right)^d \sum_{k=1}^B q_{tt}^{\beta k} \gamma_{\text{twin}} \dot{f}^k \quad (2.9)$$

where h_{ts}^0 , $q_{ts}^{\beta k}$ and e are hardening parameters for twin-slip interaction, h_{tt}^0 , $q_{tt}^{\beta k}$ and d are hardening parameters for twin-twin interaction. The exponent e leads to saturation of twin volume fraction at later stages of deformation [32]. Note that the modified CPFEM framework Eqs.(2.6, 2.1, 2.8, 2.7, 2.9) only considers the slip and twinning in untwinned region. The slip and twinning in twinned region are excluded. Since slip and twinning happen in the intermediate configuration, the conjugate stress and strain \mathbf{T}^* , \mathbf{E}^* are used instead of $\boldsymbol{\sigma}$, $\boldsymbol{\epsilon}$ for implementation.

2.2 Kinematic hardening

To account for the Bauschinger effect, a nonlinear kinematic hardening rule was proposed by Armstrong and Frederick. The evolution of the back stress $\boldsymbol{\sigma}_b$ is

$$\dot{\boldsymbol{\sigma}}_b = H_K \dot{\epsilon}^p - \gamma \dot{\epsilon}^p \boldsymbol{\sigma}_b \quad (2.10)$$

where H_K and γ are constant material parameters. Note that ϵ^p represents effective plastic strain. For uniaxial case, the back stress can be solved explicitly [18],

$$\sigma_b = \frac{H_K}{\gamma} \text{sgn}(\dot{\epsilon}^p) + \left[\sigma_{b0} - \frac{H_K}{\gamma} \text{sgn}(\dot{\epsilon}^p)\right] \exp[-\gamma(\epsilon^p - \epsilon_0^p) \text{sgn}(\dot{\epsilon}^p)] \quad (2.11)$$

where σ_{b0} and ϵ_0^p are initial stress and strain. If the loading direction reverses, σ_{b0} and ϵ_0^p need to be updated. In addition, to include the back stress in the crystal plasticity, Eq.(2.10) is changed as

$$\dot{\tau}_b^\alpha = c\dot{\gamma}^\alpha - d\dot{\gamma}^\alpha\tau_b^\alpha \quad (2.12)$$

where c and d are constant material parameters for all slip system α . Then, the slip power-law model Eq.(2.1) becomes

$$\dot{\gamma}^\alpha = \dot{\gamma}_{\text{slip}}^0 \left| \frac{\tau^\alpha - \tau_b^\alpha}{\tau_c^\alpha} \right|^{n_{\text{slip}}} \text{sgn}(\tau^\alpha - \tau_b^\alpha) \quad (2.13)$$

Thus, the modified CPFEM framework has one more variable, that is, Eqs.(2.6, 2.13, 2.8, 2.7, 2.9, 2.12). Such ODEs are solved using the ODE integration scheme (e.g. fixed-point iteration, Runge-Kutta methods) [30].

2.3 Material parameter calibration

Generally, material parameters for FEM simulation is determined by flow curve fitting using empirical isotropic hardening laws (e.g. Swift, Hockett-Sherby). However, for CPFEM, the hardening law is implicit thus cannot be determined by flow curve fitting directly. Instead, material parameters are calibrated using virtual testing, that is,

$$\min_{\mathbf{p}} O(\mathbf{p}) = \sum_i^N \left\| \sigma_i^{\text{exp}} - \sigma_i^{\text{sim}}(\epsilon_i^{\text{exp}}, \mathbf{p}) \right\|^2 \quad (2.14)$$

where \mathbf{p} a vector containing material parameters, $(\epsilon_i^{\text{exp}}, \sigma_i^{\text{exp}})_{i=1}^N$ are experimental flow curve data, $(\epsilon_i^{\text{sim}}, \sigma_i^{\text{sim}})_{i=1}^N$ are simulation results run by FEM softwares (e.g. Abaqus, MSC.Marc). The objective function $O(\mathbf{p})$ is minimized by genetic algorithm [35] [7] or response surface method [16] [28]. The common crystal plastic model for parameter calibration is the slip power-law model Eqs.(2.13, 2.2, 2.3, 2.12), which has the set of parameters,

$$\mathbf{p} = [\dot{\gamma}_{\text{slip}}^0, n_{\text{slip}}, \tau_c^0, \tau_s, h^0, a, c, d]$$

where $\dot{\gamma}_{\text{slip}}^0, n_{\text{slip}}, a$ usually takes the value 0.001, 20, 2.0. Nearly all the optimization method need an initial guess. A good initial guess can largely decrease number of objective function evaluation, which means less number of simulation. Hence, a procedure of the initial parameter guess is proposed for materials under the tension-compression test.

Due to the conservation of energy, the sum of work done by the critical resolved shear stress on each active slip system should equal to the external work,

$$\sum_{\alpha=1}^A \tau_c^\alpha \dot{\gamma}^\alpha = \boldsymbol{\sigma} : \dot{\boldsymbol{\epsilon}} \quad (2.15)$$

For uniaxial tensile test, M factor is defined as [6],

$$M = \frac{\sum_{\alpha=1}^A \dot{\gamma}^\alpha}{\dot{\epsilon}_{11}^p} \quad (2.16)$$

By Taylor's approach [34] and under the restriction that τ_c^α is constant τ_c (average value),

$$M = \frac{\sum_{\alpha=1}^A |\dot{\gamma}^\alpha|}{\dot{\epsilon}_{11}^p} = \frac{\sigma_{11}}{\tau_c} \quad (2.17)$$

Taylor's M factor usually takes the value 3.06 for fcc lattice and has the similar value for bcc lattice (i.e. 3.067 for $\{110\}\langle 111 \rangle$, 2.95 for $\{112\}\langle 111 \rangle$ [29])

The derivation of Taylor's factor M is based on isostrain assumption. Under the same assumption, the macroscopic effective elastic constants for orthotropic material is derived from the elastic tensor Eq.(1.7) using Voigt average [8],

$$E_V = \frac{(A - B + 3C)(A + 2B)}{2A + 3B + C} \quad G_V = \frac{A - B + 3C}{5} \quad \nu_V = \frac{A + 4B - 2C}{4A + 6B + 2C} \quad (2.18a)$$

$$A = \frac{c_{11} + c_{22} + c_{33}}{3} \quad B = \frac{c_{23} + c_{13} + c_{12}}{3} \quad C = \frac{c_{44} + c_{55} + c_{66}}{3} \quad (2.18b)$$

where E_V is effective Young's modulus, G_V is effective shear modulus, ν_V is effective Poisson's ratio. In particular, for fcc and bcc lattice structures,

$$E_V = \frac{(c_{11} - c_{12} + 3c_{44})(c_{11} + 2c_{12})}{2c_{11} + 3c_{12} + c_{44}}, \quad G_V = \frac{c_{11} - c_{12} + 3c_{44}}{5}, \quad \nu_V = \frac{c_{11} + 4c_{12} - 2c_{44}}{4c_{11} + 6c_{12} + 2c_{44}} \quad (2.19)$$

Consider the slip power-law model Eq.(2.1), a similar macroscopic power-law model [17] is

$$\dot{\epsilon}^p = \dot{\epsilon}^0 \left(\frac{\sigma_e}{\sigma_f} \right)^m \quad (2.20)$$

where $\dot{\epsilon}^0$ is a reference strain rate, $\sigma_f = g(\epsilon^p)$ is stress-plastic strain relation in uniaxial tension and m is the rate-sensitivity exponent which usually takes a large value (≥ 20) to weaken the strain rate dependence. With the back stress,

$$\sigma = \sigma_b + \text{sgn}(\dot{\epsilon}^p) \sigma_e \quad (2.21)$$

Eq.(2.20) yields,

$$\sigma = \sigma_b + \text{sgn}(\dot{\epsilon}^p) \left| \frac{\dot{\epsilon}^p}{\dot{\epsilon}^0} \right|^{\frac{1}{m}} \sigma_f \quad (2.22)$$

where σ_f can take any macroscopic hardening law. For instance, Hockett-Sherby hardening law has the form,

$$\sigma_f = f_1 + f_2 \left[1 - \exp \left(f_3 (\epsilon^p)^{f_4} \right) \right] \quad (2.23)$$

which indicates that $\sigma_f(0) = f_1$, $\sigma_f(\infty) = f_1 + f_2$ and $\frac{d\sigma_f}{d\epsilon^p}(0) \approx f_2 f_3$. For the uniaxial test, back stress Eq.(2.11) can be substituted into Eq.(2.22) with Eq.(2.23),

$$\begin{aligned} \sigma(\epsilon^p, \dot{\epsilon}^p, m, f_1, f_2, f_3, f_4, H_K, \gamma) = & \text{sgn}(\dot{\epsilon}^p) \left| \frac{\dot{\epsilon}^p}{\dot{\epsilon}^0} \right|^{\frac{1}{m}} \left\{ f_1 + f_2 \left[1 - \exp \left(f_3 (\epsilon^p)^{f_4} \right) \right] \right\} + \\ & \frac{H_K}{\gamma} \text{sgn}(\dot{\epsilon}^p) + \left[\sigma_{b0} - \frac{H_K}{\gamma} \text{sgn}(\dot{\epsilon}^p) \right] \exp[-\gamma (\epsilon^p - \epsilon_0^p) \text{sgn}(\dot{\epsilon}^p)] \end{aligned} \quad (2.24)$$

where $(\sigma_{b0}, \epsilon_0^p)$ starts from $(0, 0)$ and updates when the loading direction reverses (e.g. $(\sigma_{b0}, \epsilon_0^p) = (\sigma_b(\epsilon_+^p), \epsilon_+^p)$ if $\text{sgn}(\dot{\epsilon}_+^p) < 0$). Eq.(2.24) is actually the combination of Hockett-Sherby harden-

ing law with Armstrong-Frederick hardening law in the case of rate independency, which can be used to fit the stress-plastic strain flow curve of uniaxial tension-compression test. It gives the macroscopic material parameters, especially the parameters for back stress,

$$\mathbf{P} = [\dot{\epsilon}^p, m, f_1, f_2, f_3, f_4, H_K, \gamma]$$

Using the Taylor's factor Eq.(2.17),

$$\begin{aligned} \tau_c &= \frac{\sigma_{11}}{M} \\ \sum_{\alpha=1}^A |\dot{\gamma}^\alpha| &= M \dot{\epsilon}_{11}^p \\ \frac{d\tau_c}{d \sum_{\alpha=1}^A |\dot{\gamma}^\alpha|} &= \frac{1}{M^2} \frac{d\sigma_{11}}{d\dot{\epsilon}_{11}^p} \end{aligned}$$

the approximation of microscopic material parameters \mathbf{p} by macroscopic material parameters \mathbf{P} is shown in Table(3), which comes from the following analysis. Base on Eqs.(2.2, 2.3),

Macroscopic parameter	Microscopic parameter	Approximation
$\dot{\epsilon}^p$	$\dot{\gamma}_{\text{slip}}^0$	≈ 0.001
m	n_{slip}	≈ 20
f_1	τ_c^0	$\sqrt{\frac{2f_1}{\tau_c^0}} \approx M$
f_2	τ_s	$\sqrt{\frac{2(f_1+f_2)}{\tau_s}} \approx M$
f_3	h^0	$\sqrt{\frac{(f_1+f_2)f_3}{h^0}} \approx M$
f_4	a	$a \approx 2.0$
H_K	c	$\sqrt{\frac{H_K}{c}} \approx M$
γ	d	$d \approx \gamma$

Table 3: Microscopic material parameters approximated by macroscopic material parameters using Taylor's factor M

$$\dot{\tau}_c^\alpha = \sum_{k=1}^A q^{\alpha k} \left[h^0 \left(1 - \frac{\tau_c^k}{\tau_s} \right)^a \right] |\dot{\gamma}^k| \quad (2.25)$$

Assume $q^{\alpha k} \approx 1$, $a = 2.0$ and $\tau_c^k = \tau_c$ then

$$\begin{aligned} \dot{\tau}_c^\alpha &= \sum_{k=1}^A \left\{ h^0 \left[1 - 2 \frac{\tau_c^k}{\tau_s} + \left(\frac{\tau_c^k}{\tau_s} \right)^2 \right] \right\} |\dot{\gamma}^k| \\ &= h^0 \sum_{k=1}^A |\dot{\gamma}^k| - \frac{2h^0}{\tau_s} \sum_{k=1}^A \tau_c^k |\dot{\gamma}^k| + \frac{h^0}{\tau_s^2} \sum_{k=1}^A (\tau_c^k)^2 |\dot{\gamma}^k| \\ &= h^0 \sum_{k=1}^A |\dot{\gamma}^k| - \frac{2h^0}{\tau_s} \tau_c \sum_{k=1}^A |\dot{\gamma}^k| + \frac{h^0}{\tau_s^2} (\tau_c)^2 \sum_{k=1}^A |\dot{\gamma}^k| \end{aligned} \quad (2.26)$$

The Hockett-Sherby model Eq.(2.23) fulfills the following evolution equation if $f_4 = 1$,

$$\dot{\sigma}_{11} = (f_1 + f_2) f_3 \dot{\epsilon}_{11} - f_3 |\dot{\epsilon}_{11}^p| \sigma_{11} \quad (2.27)$$

Compared with Eq.(2.26) and consider the Taylor's factor,

$$\begin{aligned}\frac{2h^0}{\tau_s} &= f_3 \\ h^0 &= \frac{1}{M^2} (f_1 + f_2) f_3\end{aligned}$$

where the higher order term $\frac{h^0}{\tau_s^2} (\tau_c)^2 \sum_{k=1}^A |\dot{\gamma}^k|$ is neglected. This gives the approximation,

$$\tau_c^0 \approx \frac{2f_1}{M^2} \quad (2.28a)$$

$$\tau_s \approx \frac{2(f_1 + f_2)}{M^2} \quad (2.28b)$$

$$h^0 \approx \frac{(f_1 + f_2) f_3}{M^2} \quad (2.28c)$$

For a general flow curve model $\sigma_f(\epsilon^p)$, the approximation is proposed as

$$f_1 = \sigma_f(0) \quad (2.29a)$$

$$f_1 + f_2 = \sigma_f(\infty) \quad (2.29b)$$

$$(f_1 + f_2) f_3 = \frac{d\sigma_f}{d\epsilon^p}(0) \quad (2.29c)$$

The same routine can be applied for the back stress Eqs.(2.10, 2.12),

$$\dot{\sigma}_b = H_K \dot{\epsilon}^p - \gamma \dot{\epsilon}^p \sigma_b$$

$$\dot{\tau}_b^\alpha = c \dot{\gamma}^\alpha - d \dot{\gamma}^\alpha \tau_b^\alpha$$

which yields

$$c \approx \frac{H_K}{M^2} \quad (2.30a)$$

$$d \approx \gamma \quad (2.30b)$$

Finally, the microscopic material parameters are summarized in Table(4) where M usually in the range $[2, 3]$. The lower bound of M is given by Sachs model and the upper bound of M is given by Taylor model [6]. Note that $\tau_c^0 \approx \frac{f_1}{M}$ and $\tau_s \approx \frac{(f_1+f_2)}{M}$ are suggested by Taylor's factor directly, which are consistent with Eqs.(2.28) as $\frac{2}{M^2} \approx \frac{1}{M}$ when $M \in [2, 3]$.

$\dot{\gamma}_{\text{slip}}^0$	0.001
n_{slip}	20
τ_c^0	$\frac{2f_1}{M^2}$ or $\frac{f_1}{M}$
τ_s	$\frac{2(f_1+f_2)}{M^2}$ or $\frac{(f_1+f_2)}{M}$
h^0	$\frac{(f_1+f_2)f_3}{M^2}$
a	2.0
c	$\frac{H_K}{M^2}$
d	γ

Table 4: Material parameter approximation for slip phenomenological power-law model with Armstrong-Frederick type back stress using the parameters from Eq.(2.23) and Eq.(2.24)

The macroscopic material parameters are obtained by flow curve fitting. Assume the uniaxial tension/compression test gives the experimental data $(\epsilon_i, \sigma_i)_{i=1}^N$, which is composed of tensile data $(\epsilon_i, \sigma_i)_{i=1}^{N_+}$ and compressive data $(\epsilon_i, \sigma_i)_{i=N_++1}^N$, the strains are converted to plastic strains by

$$\epsilon_i^p = \epsilon_i - \frac{\sigma_i}{E} \quad (2.31)$$

The tension test data $(\epsilon_i, \sigma_i)_{i=1}^{N_+}$ are fit by Hockett-Sherby law Eq.(2.23),

$$\min_{\mathbf{P}^+} \sum_{i=1}^{N_+} \|\sigma_i - \sigma_f(\epsilon_i^p, \mathbf{P}^+)\|^2 \quad (2.32)$$

from which f_1, f_2, f_3, f_4 are obtained. The total tension/compression test data are fit by Eq.(2.24),

$$\min_{\mathbf{P}} \sum_{i=1}^N \|\sigma_i - \sigma(\epsilon_i^p, \mathbf{P})\|^2 \quad (2.33)$$

from which c, d are obtained. Note that $(\epsilon_{N_+}^p, \sigma_{N_+})$ is a critical point where loading direction reverses. Global optimization method (e.g. differential evolution method) is suggested in order to get an optimal result.

In conclusion, the procedure for initial microscopic material parameter guess is listed as follows,

1. Do the uniaxial tension/compression test and get the data $(\epsilon_i, \sigma_i)_{i=1}^N$, which is composed of tensile data $(\epsilon_i, \sigma_i)_{i=1}^{N_+}$ and compressive data $(\epsilon_i, \sigma_i)_{i=N_++1}^N$.
2. Calculate Young's modulus E from the tensile data $(\epsilon_i, \sigma_i)_{i=1}^{N_+}$, which should $\leq E_V$ by Eq.(2.18).
3. Fit the tensile curve $(\epsilon_i^p, \sigma_i)_{i=1}^{N_+}$ with Hockett-Sherby hardening law Eq.(2.23) and get slip hardening parameters τ_c^0, τ_s, h^0 by Eqs.(2.28).
4. Fit the whole curve $(\epsilon_i^p, \sigma_i)_{i=1}^N$ with the derived hardening law Eq.(2.24) and get back stress hardening parameters c, d by Eqs.(2.30).
5. Input the initial parameters $\mathbf{p} = [\dot{\gamma}_{\text{slip}}^0, n_{\text{slip}}, \tau_c^0, \tau_s, h^0, a, c, d]$ suggested by Table(4) to the virtual testing Eq.(2.14).

Another more practical and simpler way is to use Eq.(2.24) directly without fitting the tensile curve by Hockett-Sherby hardening law, which is listed in Table(5). The derivation comes from Eqs.(2.29) by assuming Eq.(2.24) is rate independent. This approximation is however not as good as Table(4) since the fitting of Eq.(2.24) compromises both Hockett-Sherby hardening law and Armstrong-Frederick type back stress.

2.4 Yield surface identification

The virtual testing of RVE is convenient for the yield surface identification as the boundary conditions can be set arbitrarily without considering the limitation of experimental devices. This idea is already implemented in DAMASK by [36]. Here, a homogeneous anisotropic

$\dot{\gamma}_{\text{slip}}^0$	0.001
n_{slip}	20
τ_c^0	$\frac{2f_1}{M^2}$ or $\frac{f_1}{M}$
τ_s	$\frac{2\left(f_1+f_2+\frac{H_K}{\gamma}\right)}{M^2}$ or $\frac{\left(f_1+f_2+\frac{H_K}{\gamma}\right)}{M}$
h^0	$\frac{(f_1+f_2)f_3+H_K}{M^2}$
a	2.0
c	$\frac{H_K}{M^2}$
d	γ

Table 5: Material parameter approximation for slip phenomenological power-law model with Armstrong-Frederick type back stress using the parameters from Eq.(2.24)

hardening(HAH) model which tracks the evolution of yield surface is introduced ([1],[2],[3],[26]). The yield function has stable component and fluctuating component, that is,

$$\Phi(s) = \left\{ [\phi(s)]^q + f_1^q \left| \hat{h} : s - \left| \hat{h} : s \right| \right|^q + f_2^q \left| \hat{h} : s + \left| \hat{h} : s \right| \right|^q \right\}^{\frac{1}{q}} = \sigma_r(\epsilon^p) \quad (2.34)$$

where $\phi(s)$ is an anisotropic yield function, $\sigma_r(\epsilon^p)$ is a monotonic isotropic hardening curve, s is the deviator of Cauchy stress and \hat{h} is a normalized traceless tensor called microstructure deviator. The normalization \hat{h} is defined as

$$\hat{h} = \frac{h}{\sqrt{Hh:h}} \quad (2.35)$$

and two coefficients f_1, f_2 are given by

$$f_k = \left[\frac{\sqrt{6H}}{4} \left(\frac{1}{g_k} - 1 \right) \right]^{\frac{1}{q}} \text{ for } k = 1, 2 \quad (2.36)$$

where H is a constant chosen to $H = \frac{8}{3}$ for simplicity and g_1, g_2 are two state variables. A parameter $\cos \chi$ is used to characterize the loading change, which is

$$\cos \chi = \frac{\hat{s} : \hat{h}}{\sqrt{\hat{s} : \hat{s}} \sqrt{\hat{h} : \hat{h}}} = H \hat{s} : \hat{h} \quad (2.37)$$

Furthermore, the stress deviator s can be decomposed to a coaxial part s_c parallel to h and an orthogonal part s_o normal to h ,

$$s_c = H(\hat{h} : s)\hat{h} \quad (2.38)$$

$$s_o = s - s_c \quad (2.39)$$

they are used to extend the yield function $\phi(s)$ in consideration of latent hardening and shrinking effects. Therefore, $\phi(s)$ in Eq.(2.34) is replaced by

$$\phi(s) \leftarrow \sqrt{\phi\left(s_c + \frac{1}{g_L}s_o\right)^2 + \phi\left(\frac{k_p(1-g_S)}{g_L}s_o\right)^2} \quad (2.40)$$

where g_L and g_S are two state variables controlling latent hardening and shrinking effects respectively. The evolution of state variables and microstructure deviator are governed by an ODE system:

if $s : \hat{\mathbf{h}} \geq 0$

$$\begin{aligned}\frac{dg_1}{d\epsilon^p} &= k_2 \left[k_3 \frac{\sigma_f(0)}{\sigma_f(\epsilon^p)} - g_1 \right] \\ \frac{dg_2}{d\epsilon^p} &= k_1 \frac{g_3 - g_2}{g_2} \\ \frac{dg_3}{d\epsilon^p} &= 0 \\ \frac{dg_4}{d\epsilon^p} &= k_5 (k_4 - g_4)\end{aligned}\tag{2.41}$$

if $s : \hat{\mathbf{h}} < 0$

$$\begin{aligned}\frac{dg_1}{d\epsilon^p} &= k_1 \frac{g_4 - g_1}{g_1} \\ \frac{dg_2}{d\epsilon^p} &= k_2 \left[k_3 \frac{\sigma_f(0)}{\sigma_f(\epsilon^p)} - g_2 \right] \\ \frac{dg_3}{d\epsilon^p} &= k_5 (k_4 - g_3) \\ \frac{dg_4}{d\epsilon^p} &= 0\end{aligned}\tag{2.42}$$

$$\begin{aligned}\frac{d\hat{\mathbf{h}}}{d\epsilon^p} &= k \text{sgn}(\cos \chi) \left[|\cos \chi|^{\frac{1}{R}} + g_R \right] (\hat{\mathbf{s}} - \cos \chi \hat{\mathbf{h}}) \\ \frac{dg_R}{d\epsilon^p} &= k_R [k'_R (1 - \cos^2 \chi) - g_R] \\ \frac{dg_L}{d\epsilon^p} &= k_L \left[\frac{\sigma_f(\epsilon^p) - \sigma_f(0)}{\sigma_f(\epsilon^p)} \left(\sqrt{L(1 - \cos^2 \chi) + \cos^2 \chi} - 1 \right) + 1 - g_L \right] \\ \frac{dg_S}{d\epsilon^p} &= k_S [1 + (S - 1) \cos^2 \chi - g_S]\end{aligned}\tag{2.43}$$

where g_3, g_4 are added due to the permanent softening and $\sigma_f(\epsilon^p)$ is a hardening model such as Swift law, Voce law or Kocks-Mecking dislocation density model.

In summary, the state variable vector \mathbf{g} and the microstructure deviator $\hat{\mathbf{h}}$ have the following members,

$$\begin{aligned}\mathbf{g} &= [g_1 \quad g_2 \quad g_3 \quad g_4 \quad g_L \quad g_S \quad g_R] \\ \hat{\mathbf{h}} &= [\hat{h}_1 \quad \hat{h}_2 \quad \hat{h}_3 \quad \hat{h}_4 \quad \hat{h}_5 \quad \hat{h}_6]\end{aligned}$$

and the parameter vector \mathbf{P}_{HAH} has the members,

$$\mathbf{P}_{HAH} = [k_1 \quad k_2 \quad k_3 \quad k_4 \quad k_5 \quad L \quad k_L \quad S \quad k_S \quad k \quad R \quad k_R \quad k'_R \quad q \quad k_P]$$

Note that q, k_P are parameters for the yield function $\Phi(s)$ independent of state variable evolution. Some suggested and typical values for HAH in [26] are listed in Table(6) for the parameter identification. The Initial values for state variables are given in Table(7).

In addition, Yld2000-2d is chosen as a yield function ϕ in this paper, that is

$$\phi = \left[\frac{1}{2} (|\tilde{s}'_1 - \tilde{s}'_2|^a + |2\tilde{s}''_2 + \tilde{s}''_1|^a + |2\tilde{s}''_1 + \tilde{s}''_2|^a) \right]^{\frac{1}{2}}\tag{2.44}$$

where $\tilde{s}'_1, \tilde{s}'_2$ are two eigenvalues of the linear transformation of plane stress and $\tilde{s}''_1, \tilde{s}''_2$ are

k_1	k_2	k_3	k_4	k_5	L	k_L	S	k_S	k
[20, 200]	[10, 100]	[0.1, 1]	[0.8, 1]	[1, 10]	[1, 2]	[100, 500]	[0.4, 1]	[5, 50]	[15, 150]
R	k_R	k'_R	q	k_P					
5	15	0.2	2	4					

Table 6: Suggested and typical value for HAH model parameters

g_1	g_2	g_3	g_4	g_L	g_S	g_R	$\hat{\mathbf{h}}$
1.0	1.0	1.0	1.0	1.0	1.0	0.0	$\hat{\mathbf{s}}(\epsilon^p = 0)$

Table 7: Initial value for state variables

two eigenvalues of another linear transformation of plane stress. Two linear transformations $\tilde{\mathbf{s}}' = \mathbf{L}'\boldsymbol{\sigma}$, $\tilde{\mathbf{s}}'' = \mathbf{L}''\boldsymbol{\sigma}$ contains 8 coefficients α ,

$$\mathbf{L}' = \frac{1}{3} \begin{bmatrix} 2\alpha_1 & -\alpha_1 & 0 \\ -\alpha_2 & 2\alpha_2 & 0 \\ 0 & 0 & 3\alpha_7 \end{bmatrix} \quad (2.45)$$

$$\mathbf{L}'' = \frac{1}{9} \begin{bmatrix} 8\alpha_5 - 2\alpha_3 - 2\alpha_6 + 2\alpha_4 & 4\alpha_6 - 4\alpha_4 - 4\alpha_5 + \alpha_3 & 0 \\ 4\alpha_3 - 4\alpha_5 - 4\alpha_4 + \alpha_6 & 8\alpha_4 - 2\alpha_6 - 2\alpha_4 + 2\alpha_5 & 0 \\ 0 & 0 & 9\alpha_8 \end{bmatrix}$$

The linear transformations can also be expressed in terms of the stress deviator: $\tilde{\mathbf{s}}' = \mathbf{C}'\mathbf{s}$, $\tilde{\mathbf{s}}'' = \mathbf{C}''\mathbf{s}$,

$$\mathbf{C}' = \begin{bmatrix} \alpha_1 & 0 & 0 \\ 0 & \alpha_2 & 0 \\ 0 & 0 & \alpha_7 \end{bmatrix} \quad (2.46)$$

$$\mathbf{C}'' = \frac{1}{3} \begin{bmatrix} 4\alpha_5 - \alpha_3 & 2\alpha_6 - 2\alpha_4 & 0 \\ 2\alpha_3 - 2\alpha_5 & 4\alpha_4 - \alpha_6 & 0 \\ 0 & 0 & 3\alpha_8 \end{bmatrix}$$

The eigenvalues of $\tilde{\mathbf{s}}$ are calculated by

$$\tilde{s}_1 = \frac{1}{2} \left(\tilde{s}_{xx} + \tilde{s}_{yy} + \sqrt{(\tilde{s}_{xx} - \tilde{s}_{yy})^2 + 4\tilde{s}_{xy}^2} \right) \quad (2.47)$$

$$\tilde{s}_2 = \frac{1}{2} \left(\tilde{s}_{xx} + \tilde{s}_{yy} - \sqrt{(\tilde{s}_{xx} - \tilde{s}_{yy})^2 + 4\tilde{s}_{xy}^2} \right)$$

The state variable integration is done by the forward Euler method because the step size $\delta\epsilon^p$ is usually small and the stress deviator \mathbf{s} is discrete. For higher order integration schemes such as Runge-Kutta method, a continuous function $\mathbf{s}(\epsilon^p)$ can be built by interpolating the discrete points $(\epsilon_i^p, \mathbf{s}_i)$, which is not needed for the forward Euler method.

$$\begin{aligned} \begin{bmatrix} \mathbf{g}^T \\ \mathbf{h}^T \end{bmatrix}_{k+1} &= \begin{bmatrix} \mathbf{g}^T \\ \mathbf{h}^T \end{bmatrix}_k + \begin{bmatrix} \frac{d\mathbf{g}^T}{d\epsilon^p} \\ \frac{d\mathbf{h}^T}{d\epsilon^p} \end{bmatrix}_k \delta\epsilon_k^p \\ &= \begin{bmatrix} \mathbf{g}^T \\ \mathbf{h}^T \end{bmatrix}_k + \begin{bmatrix} G(\epsilon_k^p, \mathbf{g}_k, \mathbf{h}_k, \mathbf{s}_k, \mathbf{P}_{HAH}) \\ H(\epsilon_k^p, \mathbf{g}_k, \mathbf{h}_k, \mathbf{s}_k, \mathbf{P}_{HAH}) \end{bmatrix} \delta\epsilon_k^p \end{aligned} \quad (2.48)$$

The results can be put into the yield function $\Phi(\mathbf{s})$ to get the effective stress.

As for the parameter identification, the fitting procedures are

- yield function ϕ
- isotropic hardening σ_f
- distortion hardening g, h
- HAH yield function Φ

In detail, the Yld2000-2d yield function fitting requires the yield stress ($\epsilon^p \approx 0.002$) and r value: $\sigma_0, \sigma_{45}, \sigma_{90}, \sigma_b, r_0, r_{45}, r_{90}, r_b$. The subscript means the uniaxial tensile test direction at $0^\circ, 45^\circ, 90^\circ$ with respect to the rolling direction and the biaxial test. The isotropic hardening fitting requires the uniaxial tensile test data and the HAH model fitting requires the reverse and cross-loading test data. The input and output flow chart is summarized as follows,

$$\begin{array}{ll}
 (\sigma, r)_{0,45,90,b} & \xrightarrow{\phi(\sigma)} \alpha_{1,\dots,8} \\
 (\epsilon_i^p, \sigma_i)^+ & \xrightarrow{\sigma_f} f_{1,2,3,4} \\
 (\epsilon_i^p, \sigma_i) & \xrightarrow{\Phi(s)} \mathbf{P}_{HAH}
 \end{array} \quad (2.49)$$

where $(\epsilon_i^p, \sigma_i)^+$ are uniaxial tensile test data, (ϵ_i^p, σ_i) are uniaxial tension-compression test data, $f_{1,2,3,4}$ are the parameters of Hockett-Sherby model. In particular, HAH model fitting is to solve the minimization problem,

$$\min_{\mathbf{P}_{HAH}} O(\mathbf{P}_{HAH}) = \sum_{i=1}^N \left\| \Phi(\{\epsilon^p\}_{j=1}^i, \{\sigma\}_{j=1}^i, \mathbf{P}_{HAH}) - \sigma_i \right\|^2 \quad (2.50)$$

the yield function Φ is strain path dependent or deformation history dependent. In contrast to the kinematic hardening (translation of the yield surface), HAH model distorts the yield surface. In this paper, the HAH model fitting uses Levenberg-Marquardt algorithm.

3 Implementation

DAMASK spectral solver is used for virtual test on the RVE. The load file is defined from the experimental data $(\epsilon_i^{\text{exp}}, \sigma_i^{\text{exp}})_{i=1}^N$. By choosing an appropriate rate of deformation gradient $\dot{\mathbf{F}}_{BC}$, we can define two load cases, one is uniaxial tension, another is uniaxial compression. Without loss of generality, they are defined as

$$\begin{aligned} \text{fdot } \dot{\lambda}_+ & \quad 0 \quad 0 \quad 0 \quad * \quad 0 \quad 0 \quad 0 \quad * \quad P \quad * \quad * \quad * \quad * \quad 0 \quad * \quad * \quad * \quad 0 \quad t = \frac{\lambda_{N+}}{\dot{\lambda}_+} \quad N = \lceil t \rceil \\ \text{fdot } \dot{\lambda}_- & \quad 0 \quad 0 \quad 0 \quad * \quad 0 \quad 0 \quad 0 \quad * \quad P \quad * \quad * \quad * \quad * \quad 0 \quad * \quad * \quad * \quad 0 \quad t = \frac{\lambda_N - \lambda_{N+}}{\dot{\lambda}_-} \quad N = \lceil t \rceil \end{aligned}$$

with the stretch ratio $\lambda = \exp(\epsilon^{\text{exp}})$. $N+$ denotes the point at which the loading direction reverses. dropgussing can be appended at the end of the second load case as the loading direction changes. The objective function in Eq.(2.14) is modified as

$$\min_{\mathbf{p}} O(\mathbf{p}) = \sum_i^N \|\tilde{\sigma}_i^{\text{exp}}(\epsilon_i^{\text{sim}}, \mathbf{P}) - \sigma_i^{\text{sim}}(\epsilon_i^{\text{sim}}, \mathbf{p})\|^2 \quad (3.1)$$

where $\tilde{\sigma}_i^{\text{exp}}$ is the fitting of experimental data and $\epsilon_i^{\text{sim}} \in \text{Range}(\epsilon^{\text{exp}})$. Here, the simulation is executed by DAMASK spectral solver. The optimization changes the material parameters in material.config file at each iteration. The initial parameter guess is essential for DAMASK simulation since a bad start will cause the convergence failure and stop the continual running of optimization method. Therefore, the procedure mentioned in Section(2.3) is used to assist the material parameter calibration. Namely, to obtain the macroscopic material parameters \mathbf{P} from Eq.(2.33),

$$\min_{\mathbf{P}} \sum_{i=1}^N \|\sigma_i - \sigma(\epsilon_i^p, \mathbf{P})\|^2$$

with σ in Eq.(2.22),

$$\sigma = \sigma_b + \text{sgn}(\dot{\epsilon}^p) \left| \frac{\dot{\epsilon}^p}{\dot{\epsilon}^0} \right|^{\frac{1}{m}} \sigma_f$$

where ϵ_i^p and σ_i are plastic strain and stress calculated from Eq.(2.31). If σ_f is Hockett-Sherby hardening law and σ_b is Armstrong-Frederick type back stress, then Eq.(2.22) becomes Eq.(2.24). By the approximation from Table(5), the initial parameters for objective function in Eq.(3.1) are obtained. Global optimization (e.g. differential evolution) is suggested for flow curve fitting while Gradient-less method (e.g. trust region method, simplex method) is suggested for DAMASK optimization.

3.1 Uniaxial tension-compression test

The experimental data extracted from [4] are taken as generic example for uniaxial tension-compression test. The data are converted to the plastic strain/stress form by Eq.(2.31) and the effective plastic strain/effective stress form is shown in Fig.(1), which illustrates the decrease of yield strength when the tension becomes the compression. This phenomenon is predicted by the Bauschinger effect. Then the experimental data are fit by the following

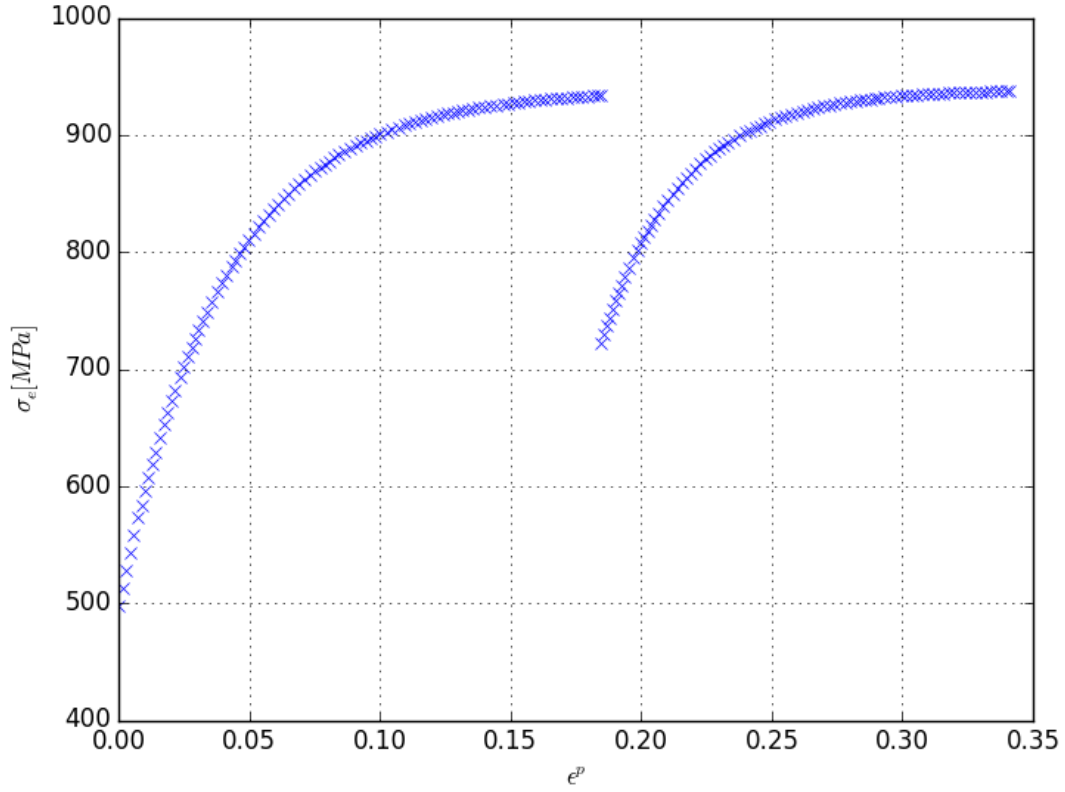


Figure 1: Experimental data in the effective plastic strain/effective stress form

hardening law from Eq.(2.24).

$$\sigma(\epsilon^p, \dot{\epsilon}^p, m, f_1, f_2, f_3, f_4, H_K, \gamma) = \text{sgn}(\dot{\epsilon}^p) \left| \frac{\dot{\epsilon}^p}{\dot{\epsilon}_0} \right|^{\frac{1}{m}} \left\{ f_1 + f_2 \left[1 - \exp \left(f_3 (\epsilon^p)^{f_4} \right) \right] \right\} + \frac{H_K}{\gamma} \text{sgn}(\dot{\epsilon}^p) + \left[\sigma_{b0} - \frac{H_K}{\gamma} \text{sgn}(\dot{\epsilon}^p) \right] \exp \left[-\gamma (\epsilon^p - \epsilon_0^p) \text{sgn}(\dot{\epsilon}^p) \right]$$

Using differential evolution method for the objective function Eq.(2.33), the bounds for each parameter are set by Table(8). There is no particular requirement for the bounds setting

$\dot{\epsilon}^p$	m	f_1	f_2	f_3	f_4	H_K	γ
[0, 0.1]	[0, 1e4]	[0, 1e4]	[0, 1e4]	[0, 1e4]	[0, 1]	[0, 1e5]	[0, 1e2]

Table 8: Parameter bounds setting for the flow curve fitting

as long as the bounds are reasonable and large enough. After that, the optimization yields the results in Table(9), which shows the rate independence as exponent $m = 4.83\text{e}3$ is large.

$\dot{\epsilon}^p$	m	f_1	f_2	f_3	f_4	H_K	γ
7.87e-2	4.83e3	499.77	238.35	16.29	0.93	6.13e3	29.73

Table 9: Optimal parameters of the hardening law in Eq.(2.24) for the uniaxial tension-compression test

Fig.(2) is the fitting curve compared with experimental data. The fitting is accurate and nearly captures all the features of original data. Thus the results can be used in $\tilde{\sigma}_i^{\text{exp}}$ of Eq.(3.1) for

DAMASK optimization.

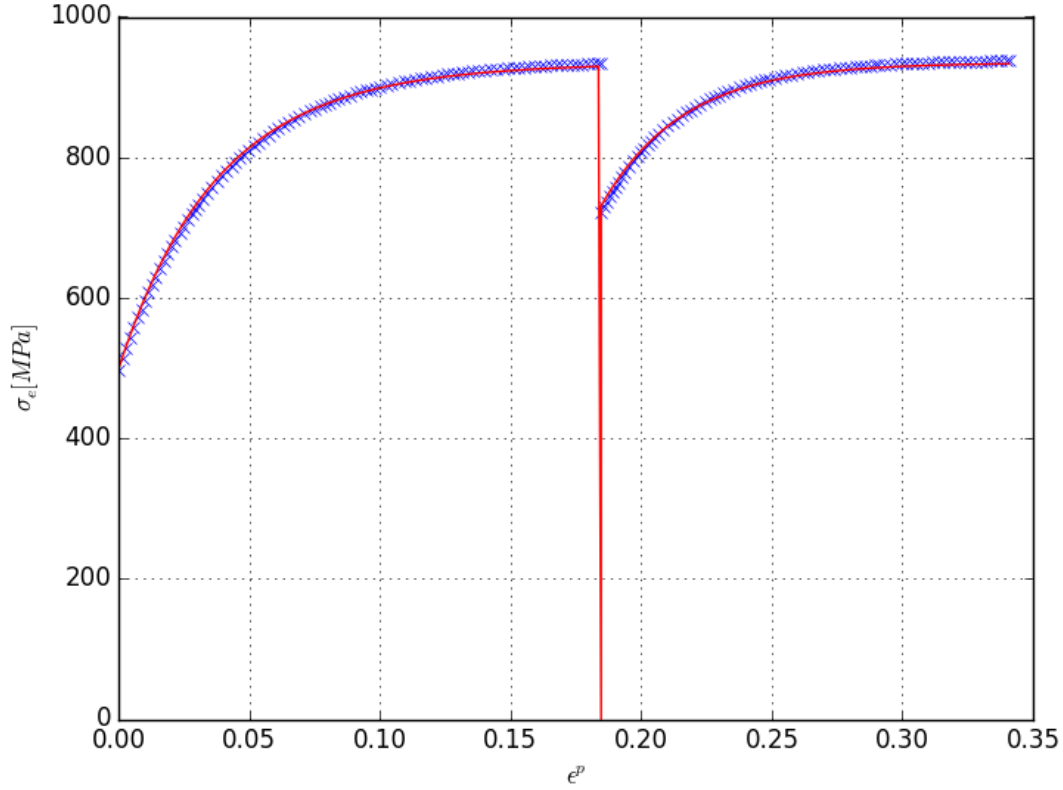


Figure 2: Curve fitting by using differential evolution method for the objective function in Eq.(2.33)

As for the virtual test, the RVE has size $1 \times 1 \times 1$ with 20 grains discretized by $8 \times 8 \times 8$ grid. By choosing the rate of stretch ratio as $2e-3$, the load file is set as,

```
fdot    2e-3  0  0  0  *  0  0  0  *  P  *  *  *  *  0  *  *  *  0  t = 99  N = 99
fdot   -2e-3  0  0  0  *  0  0  0  *  P  *  *  *  *  0  *  *  *  0  t = 87  N = 87
```

We take the elastic constants $c_{11} = 233.3e9$, $c_{12} = 135.5e9$, $c_{44} = 118.0e9$ from DAMASK material configuration files for ferrite (bcc). The Young's modulus calculated from the experimental data should less than the effective Young's modulus calculated from Eq.(2.18) due to the isostrain assumption. In fact, the elastic constants can also be included in the optimization [35] but the uniaxial test cannot provide the information of shear modulus or Poisson's ratio, which leads to unguaranted results.

Put the macroscopic material parameters into Table(5) and find a good Taylor's M factor in the range $[2, 3]$ for DAMASK simulation. A good Taylor's M factor for this example is 2.4, which is indicated by the error versus M factor in the Fig.(3). It can be seen that M factor largely influences the error (objective function value). The approximated microscopic material parameters are listed in Table(10). M factor gives a good start for local optimization.

Using the Trust Region Reflective least square method, the local optimization near $M = 2.4$ yields the optimal results in the Table(11), and the consequence flow curve is plot in Fig.(4).

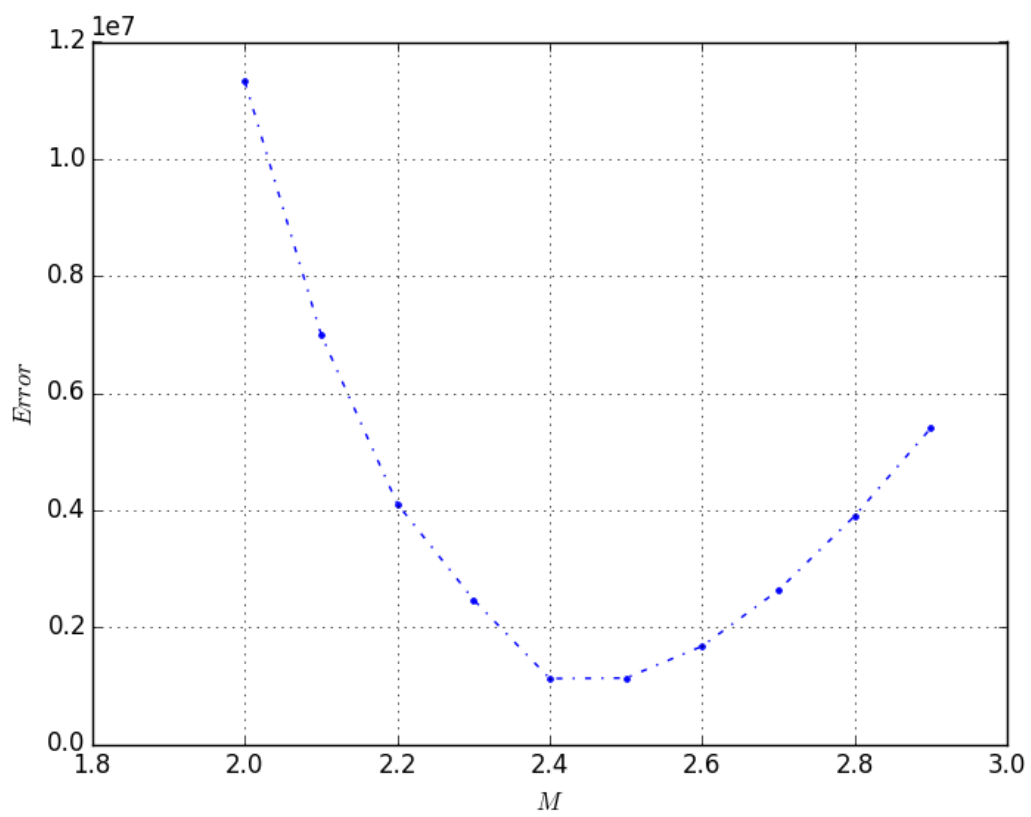


Figure 3: Error (objective function value) versus Taylor's M factor for uniaxial tension-compression test

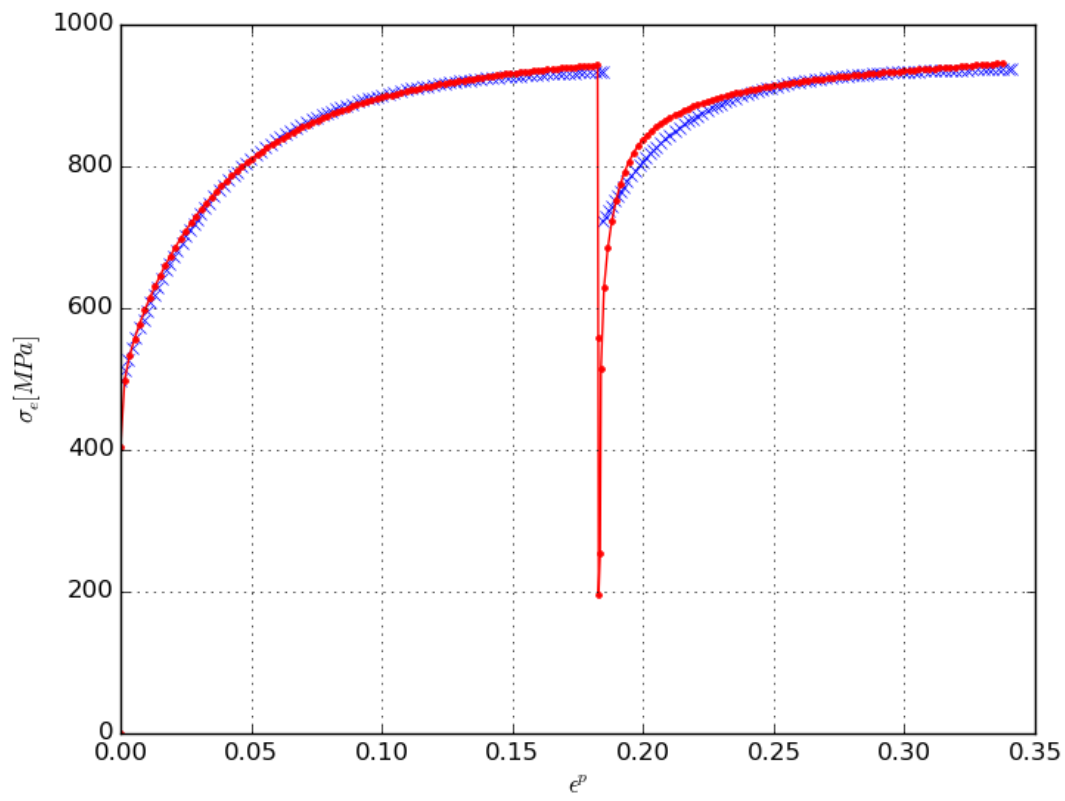


Figure 4: Uniaxial tension-compression flow curve result from Trust Region Reflective least square method

$\dot{\gamma}_{\text{slip}}^0$	0.001
n_{slip}	20
τ_c^0 (MPa)	$\frac{f_1}{M} = \frac{499.77}{2.4} = 208.24$
τ_s (MPa)	$\frac{f_1 + f_2 + \frac{H_K}{\gamma}}{M} = \frac{499.77 + 238.35 + \frac{6.13e3}{29.73}}{2.4} = 393.46$
h^0 (MPa)	$\frac{(f_1 + f_2)f_3 + H_K}{M^2} = \frac{(499.77 + 238.35)16.29 + 6.13e3}{2.4^2} = 3.15e3$
a	2.0
c (MPa)	$\frac{H_K}{M^2} = \frac{6.13e3}{2.4^2} = 1.06e3$
d	$\gamma = 29.73$

Table 10: Material parameter approximation example ($M = 2.4$)

$\dot{\gamma}_{\text{slip}}^0$	6e-3
n_{slip}	15
τ_c^0 (MPa)	225.22{110}<111>, 207.95{112}<111>
τ_s (MPa)	388.10{110}<111>, 384.47{112}<111>
h^0 (MPa)	3.61e3
a	1.25
c (MPa)	1.22e3
d	39.92

Table 11: Material parameter calibration using Trust Region Reflective least square method for uniaxial tension-compression test

In addition, the slip phenomenological power-law model without back stress implemented in Eq.(2.1) gives the flow curve in Fig.(5). It shows a good agreement under the tensile region but is not flexible under the compressive region where the curve tends to stick with the uniaxial tensile curve.

For a general test, if the data are not good fitted, macroscopic material parameters can be obtained from Eq.(2.29). Convert the data in the effective plastic strain/effective stress form and use the interpolation for $\tilde{\sigma}_i^{\text{exp}}$ in Eq.(3.1), the optimization can be done using the same routine. Note that Trust Region Reflective least square method is used for this example other than commonly used simplex method because it searches the solution in a user-defined region, which gives a reasonable result. In particular, the critical slip resistance τ_c and saturation slip resistance τ_s do not differ much between {110}<111> and {112}<111>.

3.2 Simple shear-reverse shear test

The experimental data extracted from [27] with its fitting are plot in Fig.(6). Note that the shear stress is σ_{21} and the shear strain $\gamma = 2\epsilon_{21}$. The macroscopic material parameters are listed in Table(12),

$\dot{\epsilon}^p$	m	f_1	f_2	f_3	f_4	H_K	γ
9.19e-1	6.91e3	60.59	182.58	4.13	0.82	7.35e3	295.18

Table 12: Optimal parameters of the hardening law in Eq.(2.24) for the simple shear-reverse shear test

For the virtual test, the RVE has size $1 \times 1 \times 1$ with 20 grains discretized by $8 \times 8 \times 8$ grid. The material configuration file of DAMASK for aluminum (fcc) is used. The elastic constants

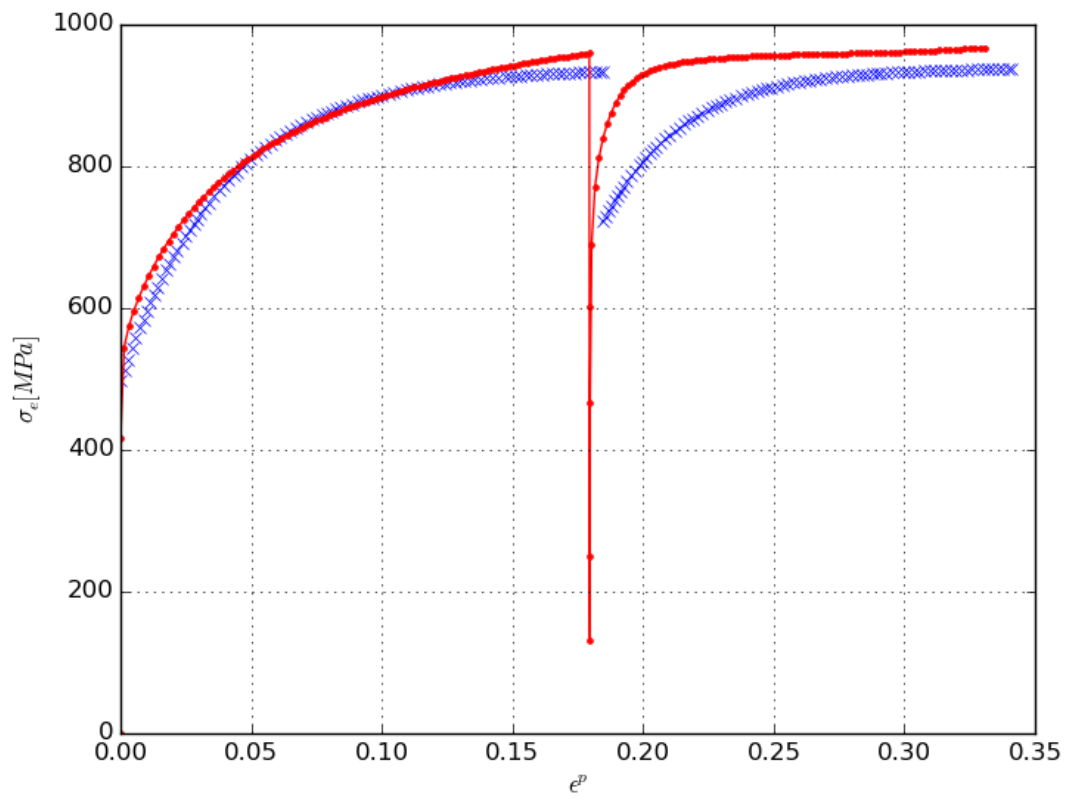


Figure 5: Uniaxial tension-compression flow curve without back stress implemented in plastic phenomenological power-law model

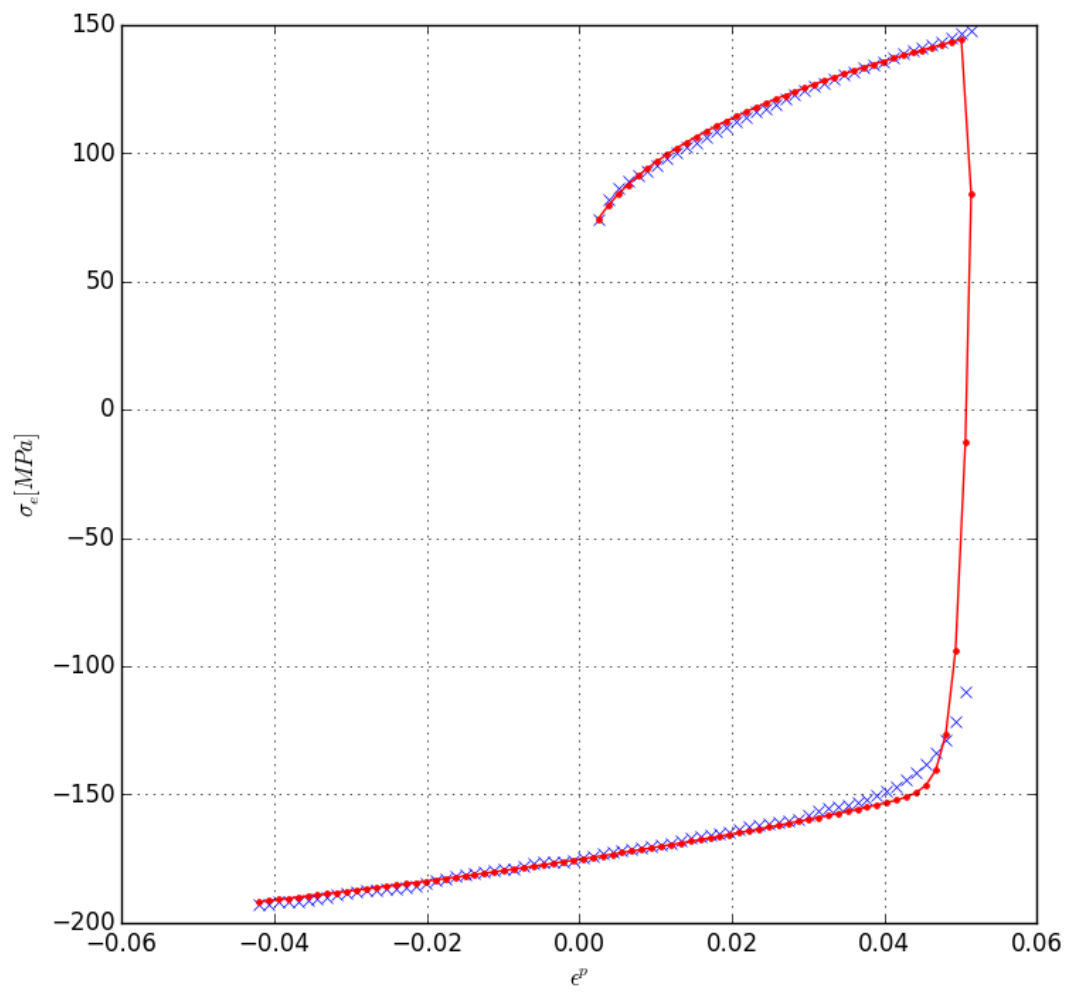


Figure 6: Shear-reverse shear test and its fitting

are $c_{11} = 106.75e9$, $c_{12} = 60.41e9$, $c_{44} = 28.34e9$. The load cases are defined as

```
fdot  0  0  0   1e-3  0  0  0  0  0  0  P  *  *  *  *  *  *  *  *  *  *  t = 100  N = 100
fdot  0  0  0  -1e-3  0  0  0  0  0  0  P  *  *  *  *  *  *  *  *  *  *  t = 190  N = 190
```

From Fig.(7), it is indicated that the optimal Taylor's M factor is around $M = 2$. Thus, the local optimization near this point gives the optimal results by Trust Region Reflective least squares method, which are listed in Table(13). Note that the stress becomes σ_{21} and the strain becomes ϵ_{21} in the objective function of Eq.(2.33). From Table(13), the exponent

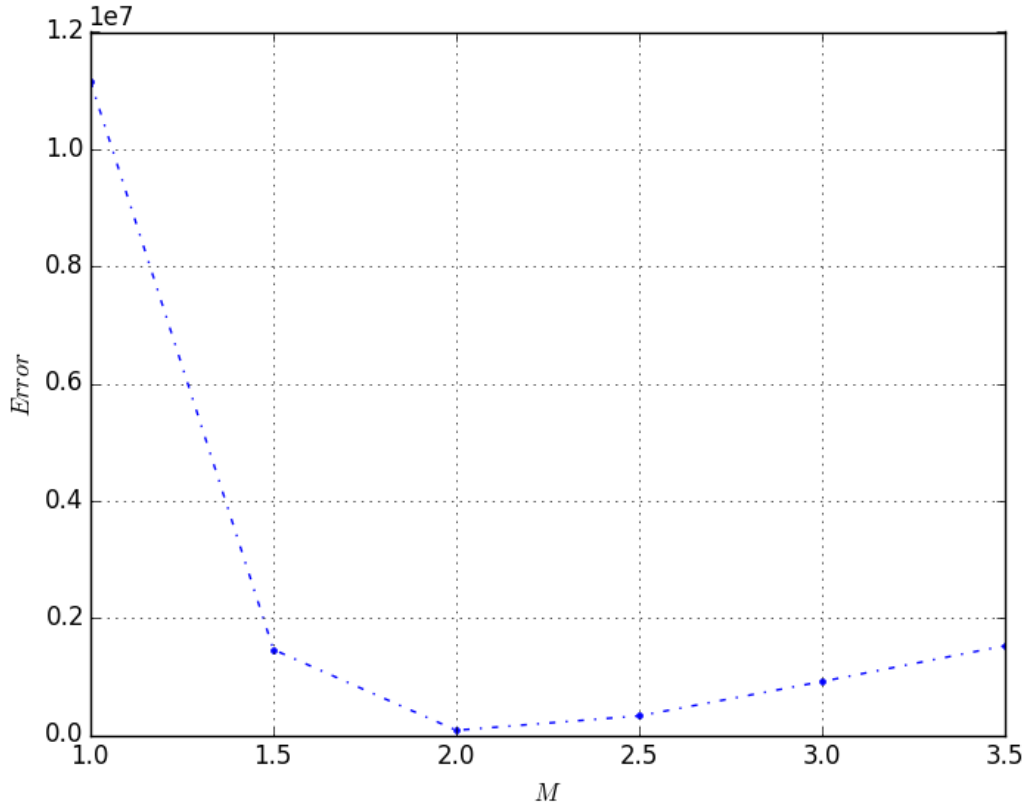


Figure 7: Error (objective function value) versus Taylor's M factor for simple shear-reverse shear test

$\dot{\gamma}_{\text{slip}}^0$	9e-4
n_{slip}	7.39
$\tau_c^0(\text{MPa})$	50.10{110}<111>
$\tau_s(\text{MPa})$	167.97{110}<111>
$h^0(\text{MPa})$	1e3
a	2.11
$c(\text{MPa})$	1.38e3
d	554.02

Table 13: Material parameter calibration for simple shear-reverse shear test using Trust Region Reflective least square method

$n_{\text{slip}} = 7.39$ indicates the rate-dependence of simple shear, which is analogous to Newton's shear law in fluid dynamics. The flow curve from the virtual test is plot with experimental data

in Fig.(8).

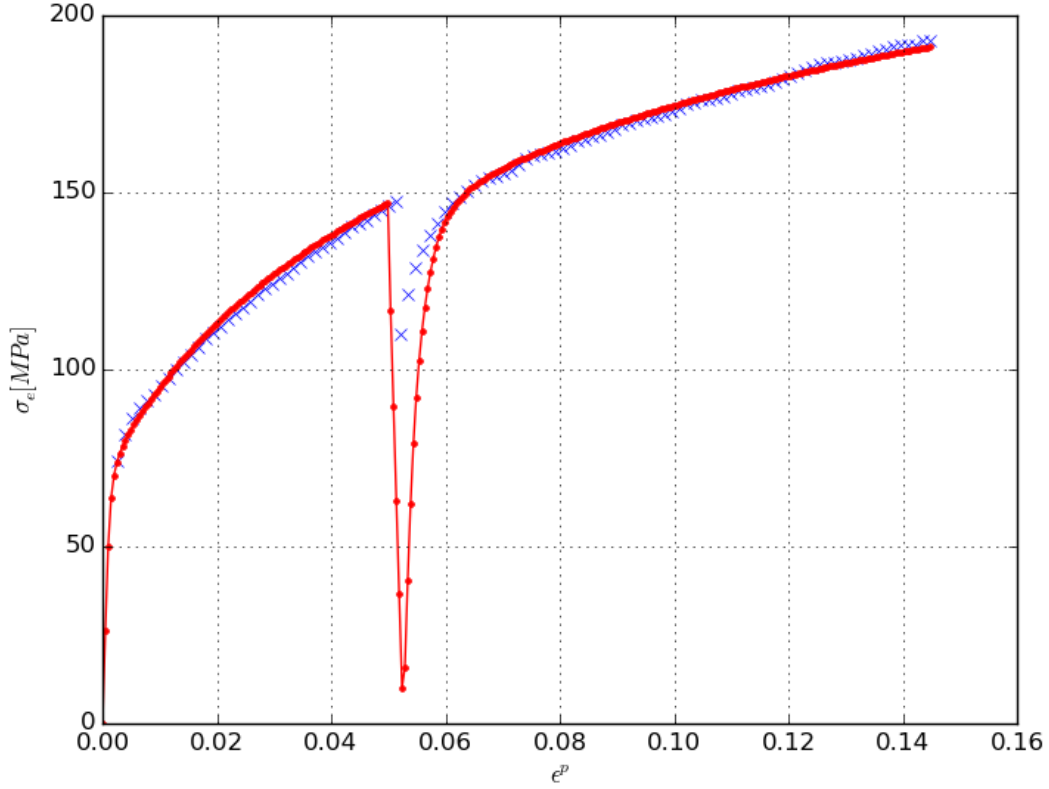


Figure 8: Simple shear-reverse shear flow curve result from Trust Region Reflective least square method

The HAH model is used to fit the simple shear-reverse shear flow curve in [27]. The parameters are listed in Table(14,15,16). In the simple shear-reverse shear case, the non-

$f_1(\text{MPa})$	$f_2(\text{MPa})$	f_3	f_4
127.63	306.65	5.26	0.84

Table 14: Hockett-Sherby model parameters fit from the uniaxial tensile flow curve [27]

σ_0	σ_{45}	σ_{90}	σ_b	r_0	r_{45}	r_{90}	r_b
147.7	144.9	146.6	130.0	0.72	0.74	0.71	1.13
α_1	α_2	α_3	α_4	α_5	α_6	α_7	α_8
0.978	1.020	1.290	1.078	1.063	1.227	1.012	0.911

Table 15: Yld2000-2d input data and fit parameters [27]

zero terms in the Cauchy stress σ are $\sigma_{21} = \sigma_{12}$ and the non-zero term in the strain tensor ϵ is ϵ_{21} . Thus, the relation between σ_{21} and the yield function ϕ can be obtained by substituting the stress tensor σ into the Yld2000-2d yield function $\phi(\sigma)$ in Eq.(2.44),

$$\sigma_r = |\sigma_{21}| \left[\frac{(2|\alpha_7|)^a + (2|\alpha_8|)^a}{2} \right]^{\frac{1}{a}} \quad (3.2)$$

In this example, $\alpha_7 = 1.012$, $\alpha_8 = 0.911$, $a = 8$ cause $|\sigma_{21}| = \frac{\sigma_r}{1.941}$ and the equivalent plastic

k_1	k_2	k_3	k_4	k_5	L	k_L	S	k_S	k
250	10.0	0.10	0.9	10.0	1.0	0	1.35	100.0	30.0
R	k_R	k'_R	q	k_P					
5	15	0.2	2	4					

Table 16: HAH model parameters for the simple shear-reverse shear flow curve [27]

strain $\epsilon^p = |\epsilon_{21}^p|$ for the state variable integration. As a result, The simple shear-reverse shear flow curves given by DAMASK virtual test and HAH model are plot in Fig.(9). To compare with

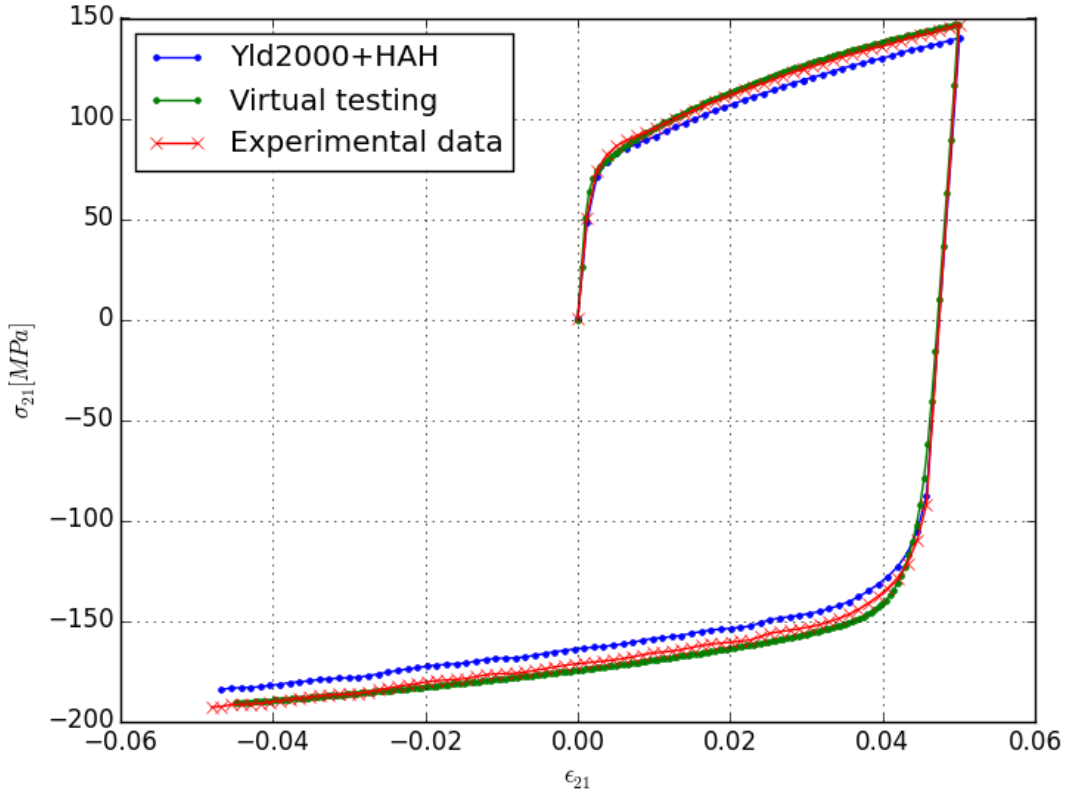


Figure 9: simple shear-reverse shear flow curve from experimental test, fit by DAMASK virtual test and HAH model

the HAH model, the virtual tests along different angles with respect to the rolling direction(X direction for RVE) are run by DAMASK. The flow curves are plot in Fig.(10). In particular, the virtual uniaxial tensile curve is extracted in comparison with the experimental data fit by Hockett-Sherby law whose parameters are listed in Table(14). From Fig.(11), the uniaxial tensile curve predicted by the virtual test follows the Hockett-Sherby law basically, but the difference exists in the yield stress and curvature. The error may come from different grain textures of the RVE and the experimental specimen. It is possible to reduce the error by material calibration for the uniaxial tensile curve.

Moreover, the yield stresses and r values from the virtual test and experimental test for the Yld2000-2d yield locus fitting are listed in Table(17). It shows that the flow stress in the rolling direction(0°) is nearly equal to the flow stress in the transverse direction(90°), which can also be observed from the flow curves in Fig.(10). Besides, the r values differ between experimental test and virtual test, which is also mentioned in [21]. The outcome yield loci

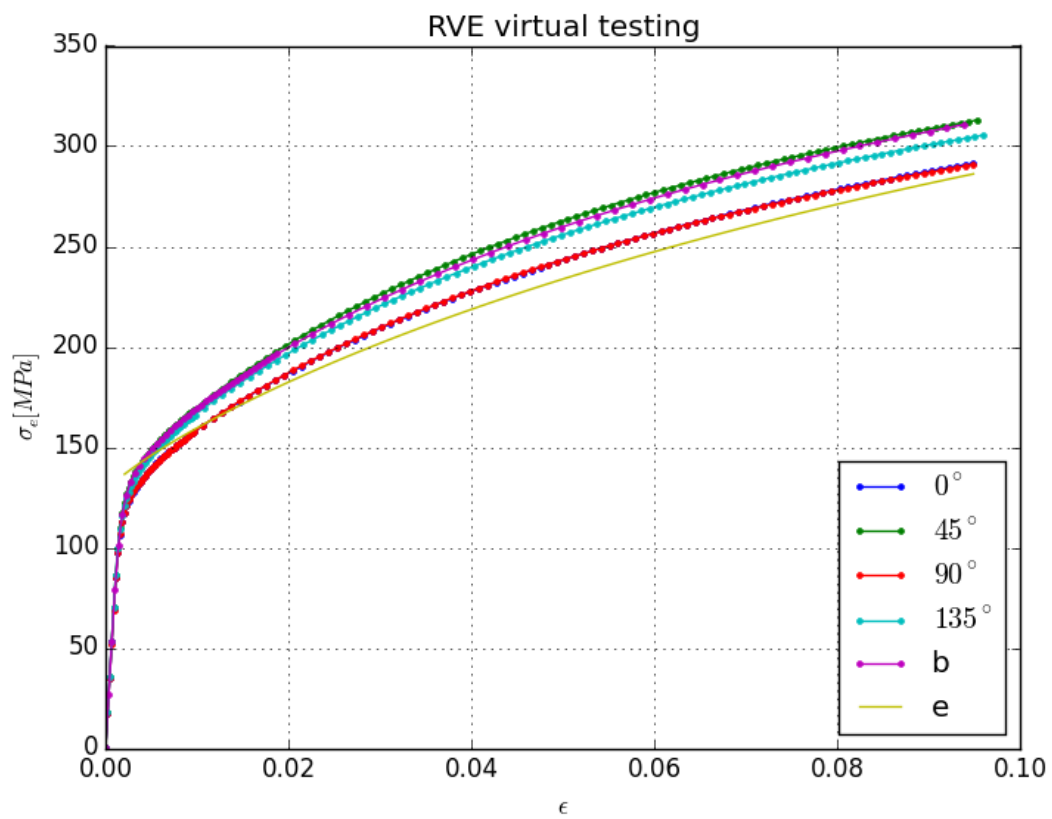


Figure 10: RVE virtual uniaxial and biaxial tensile test: the angles are with respect to the rolling direction(X direction for RVE), the symbol 'b' denotes the biaxial test and the symbol 'e' denotes the experimental data fit by Hockett-Sherby law with parameters in Table(14)

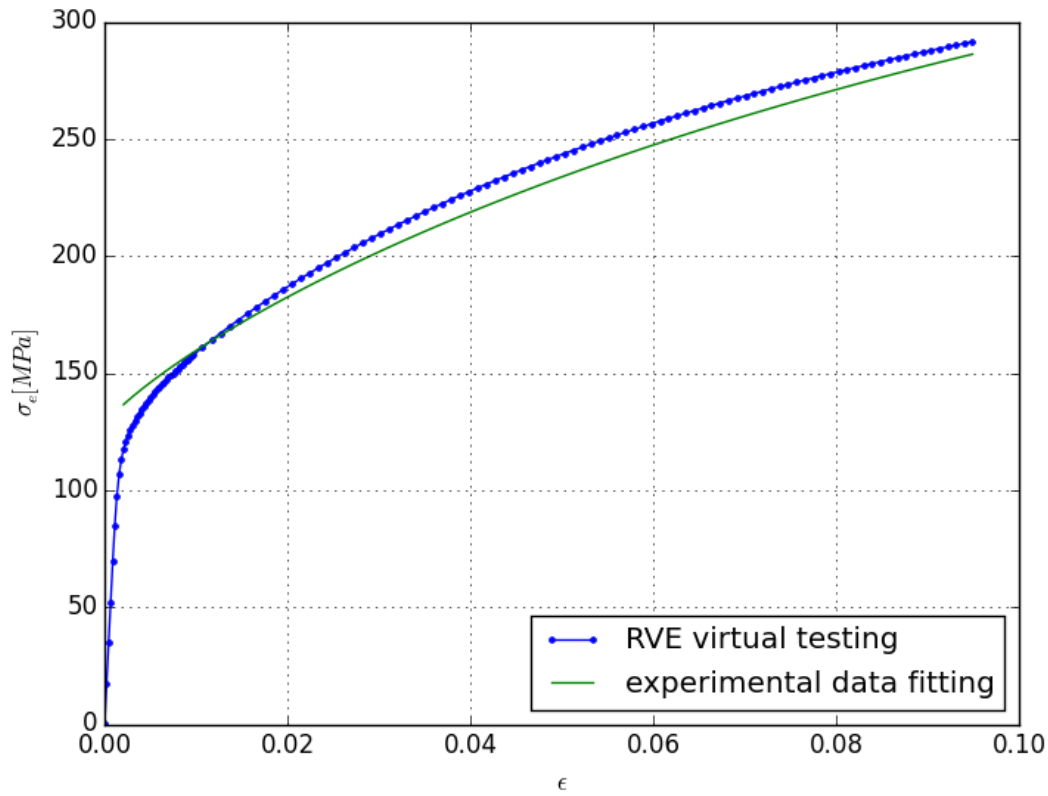


Figure 11: RVE virtual uniaxial tensile test vs experimental data fit by Hockett-Sherby law

are plot in Fig.(12), especially, $(0, \sigma_0)$, $(\sigma_{90}, 0)$, (σ_b, σ_b) , $(\sigma_{21}, -\sigma_{21})$ are marked in the plane of principal stress. The principal values of shear-reverse shear test in the fourth quadrant shows that the yield locus generated by the virtual test are more consistent than the one generated by the experimental test.

	σ_0	σ_{45}	σ_{90}	σ_b	r_0	r_{45}	r_{90}	r_b
experimental test	147.7	144.9	146.6	130.0	0.72	0.74	0.71	1.13
virtual test	117.3	122.6	117.6	121.1	1.05	0.63	0.99	1.0

Table 17: Yld2000-2d input data: virtual test vs experimental test[27]

As the uniaxial tension-compression test cannot be realized on the metal sheet, the flow curve is predicted by the virtual test in Fig.(13). The parameters of HAH model are obtained by the fitting of simple shear-reverse shear experiment data. The equivalent stress of HAH model agrees with von Mises stress during tension but differs during compression. It indicates that HAH model depends on the strain path and its parameters will change according to the strain path. In addition, the evolution of the yield surface is plot in Fig.(14) which shows the hardening and distortion of the surface. Although the HAH model can capture the Baushinger effect of uniaxial tension-compression test, it can not show the Baushinger effect of shear-reverse shear test. For the shear-reverse shear test, the evolution of the yield surface is only isotropic hardening.

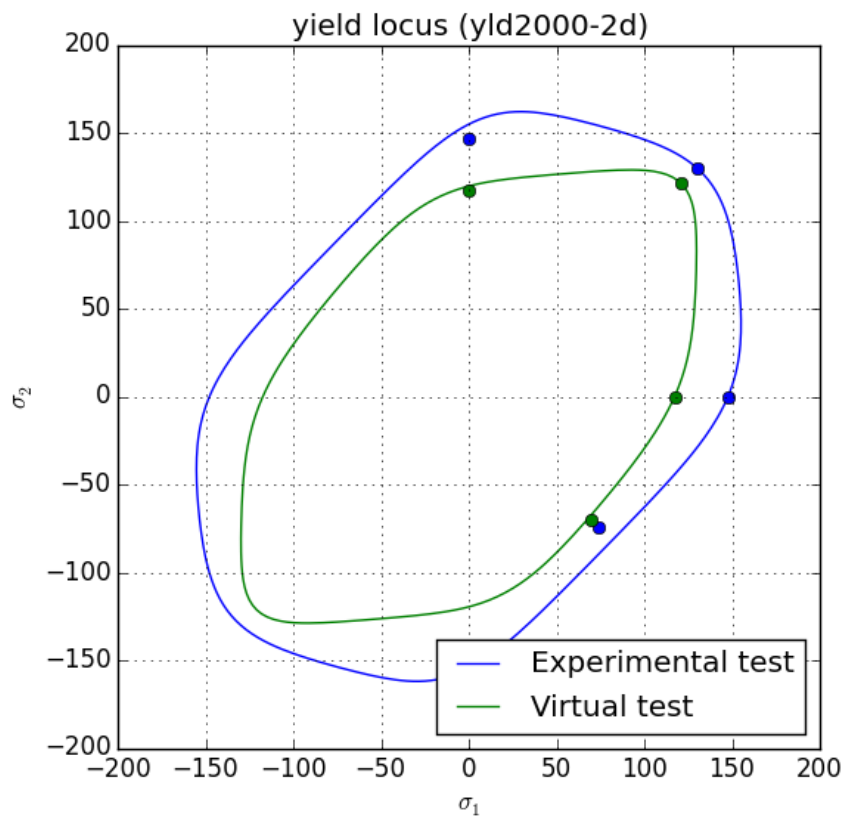


Figure 12: Yld2000-2d yield loci: virtual test vs experimental test

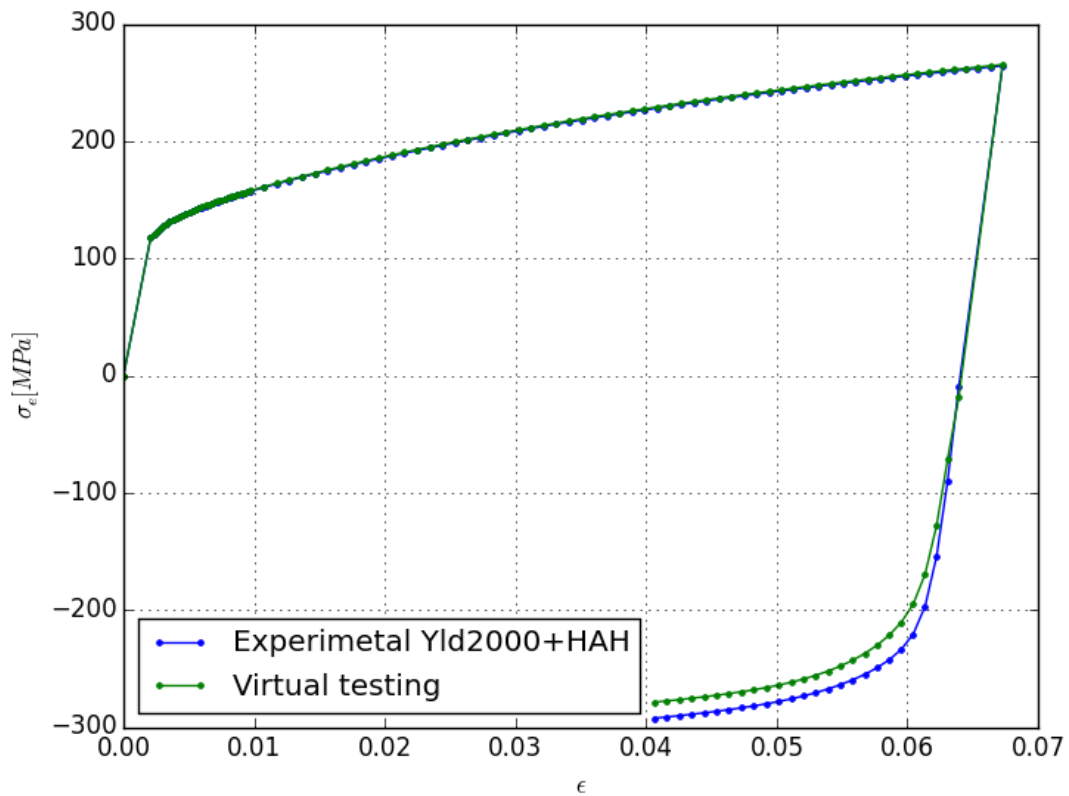


Figure 13: Virtual uniaxial tension-compression test: equivalent stress of HAH model vs von Mises stress

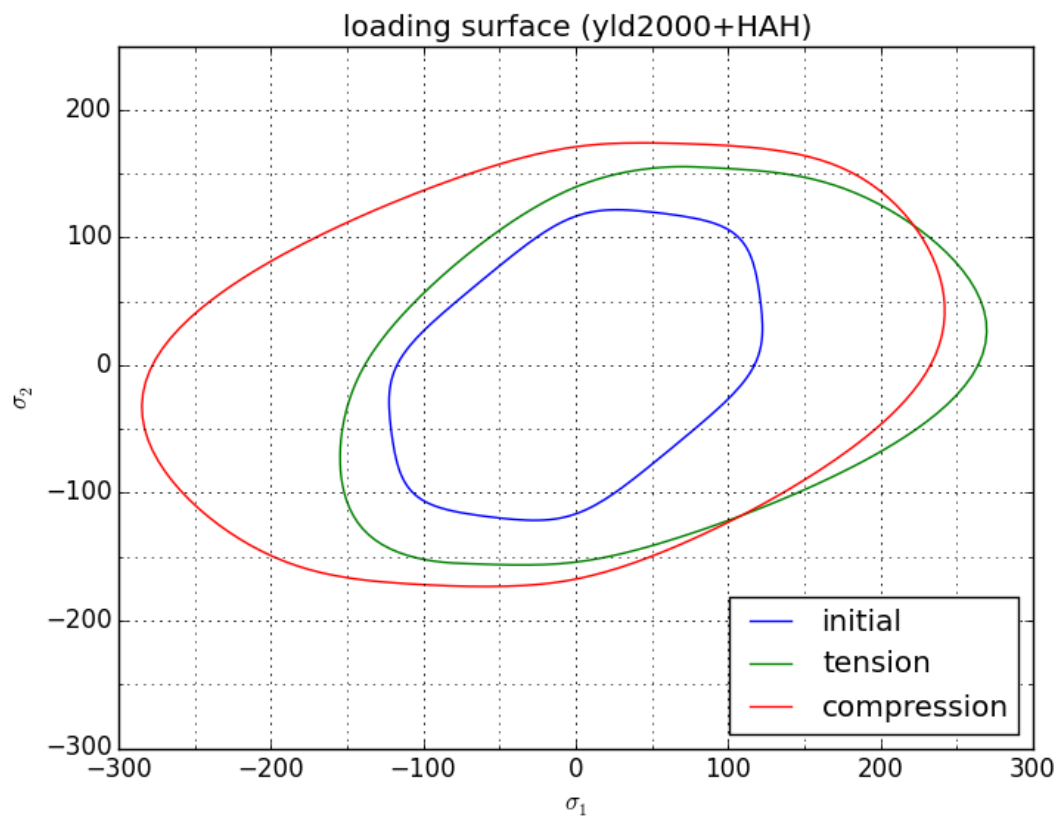


Figure 14: Evolution of yield surface by HAH model: the green one is at the end of tension loading and the red one is at the end of compression

3.3 Virtual test

The loading condition which is not achievable in reality can be realized by the virtual test. In this case, the virtual test is applied for the yield surface fitting. RVE has 20 grains and $8 \times 8 \times 8$ discretization. The test material is aluminium and its material configuration file follows DAMASK. Some of the parameters are modified by the calibration in Table(13). As an example, the uniaxial tension-compression test fit by HAH model is plot in Fig.(15), where

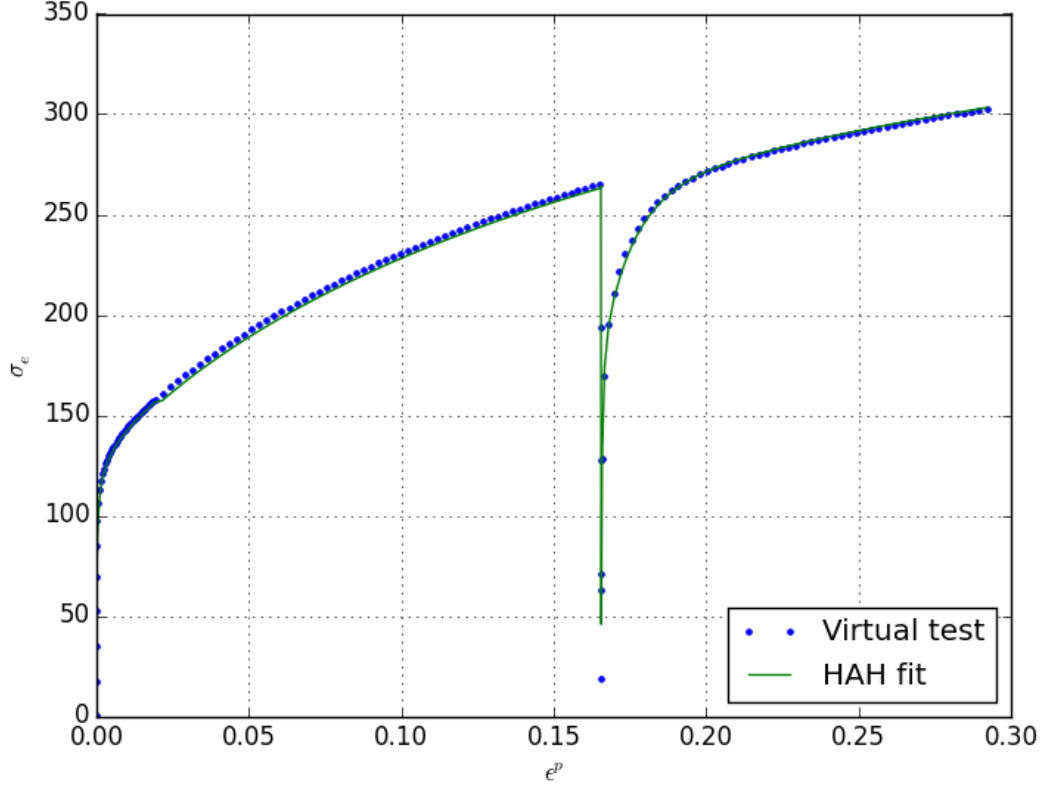


Figure 15: Virtual uniaxial tension-compression test fit by HAH model

the uniaxial tension data fit by the Hockett-Sherby law yield the coefficients in Table(18) and the fit coefficients of Yld2000-2d are given in Table(19).

$f_1(\text{MPa})$	$f_2(\text{MPa})$	f_3	f_4
120.03	250.99	3.3	0.79

Table 18: Hockett-Sherby model parameters fit from the virtual uniaxial tension test

σ_0	σ_{45}	σ_{90}	σ_b	r_0	r_{45}	r_{90}	r_b
117.3	122.6	117.6	121.1	1.05	0.63	0.99	1.0
α_1	α_2	α_3	α_4	α_5	α_6	α_7	α_8
1.149	0.708	0.878	1.003	0.987	0.952	1.0	1.0

Table 19: Yld2000-2d input data and fit parameters based on the virtual tests

For the HAH model fitting, the load case of the virtual test is set to be the plane stress so that the yield locus can be plot in the principal stress plane. The material is prestrained

to 0.05 first and then undergoes different plane stress state. The strain rate is chosen to be $\dot{\lambda} = 1e-3$ and has components $\dot{\lambda} \cos \theta$, $\dot{\lambda} \sin \theta$ in x, y directions. For instance, pick $\theta = 45^\circ$, then the load case is set by

```
fdot  1e-3  0  *  0      0  *  0  0  *  P  *  *  0  *  *  0  *  *  0  t = 10  N = 40
fdot  1e-3  0  *  0      0  *  0  0  *  P  *  *  0  *  *  0  *  *  0  t = 40  N = 40
fdot  0.7e-3  0  *  0  0.7e-3  *  0  0  *  P  *  *  0  *  *  0  *  *  0  t = 10  N = 40
fdot  0.7e-3  0  *  0  0.7e-3  *  0  0  *  P  *  *  0  *  *  0  *  *  0  t = 40  N = 40
```

the small time step $\frac{t}{N}$ at the beginning of loading or when the loading direction changes is to capture the drastic strain-stress curvature change. Take θ to be $36^\circ, 72^\circ, \dots, 214^\circ, 0^\circ, 45^\circ, 90^\circ, \dots, 315^\circ$, the principal stress points corresponding to the total shear strain $\epsilon^p \approx 0.2$ are plot in Fig.(16). The Yld2000-2d + HAH model fitting is depicted in Fig.(17). The initial input for the least square method is listed in Table(16) where parameters R , k_R , k'_R , q , k_P are kept constant and others are variables. The fit parameters are listed in Table(20). Note that parameter k_4 is sensitive to the permanent softening. $k_4 = 1.0$ for pure hardening. The fit parameters change significantly when the loading direction inverses($\theta = 180^\circ, 216^\circ$) because the information of tension and compression is complete and the change from tension to compression is significant in those cases. As a result, Fig.(17e) and Fig.(17f) predict all the stress points well.

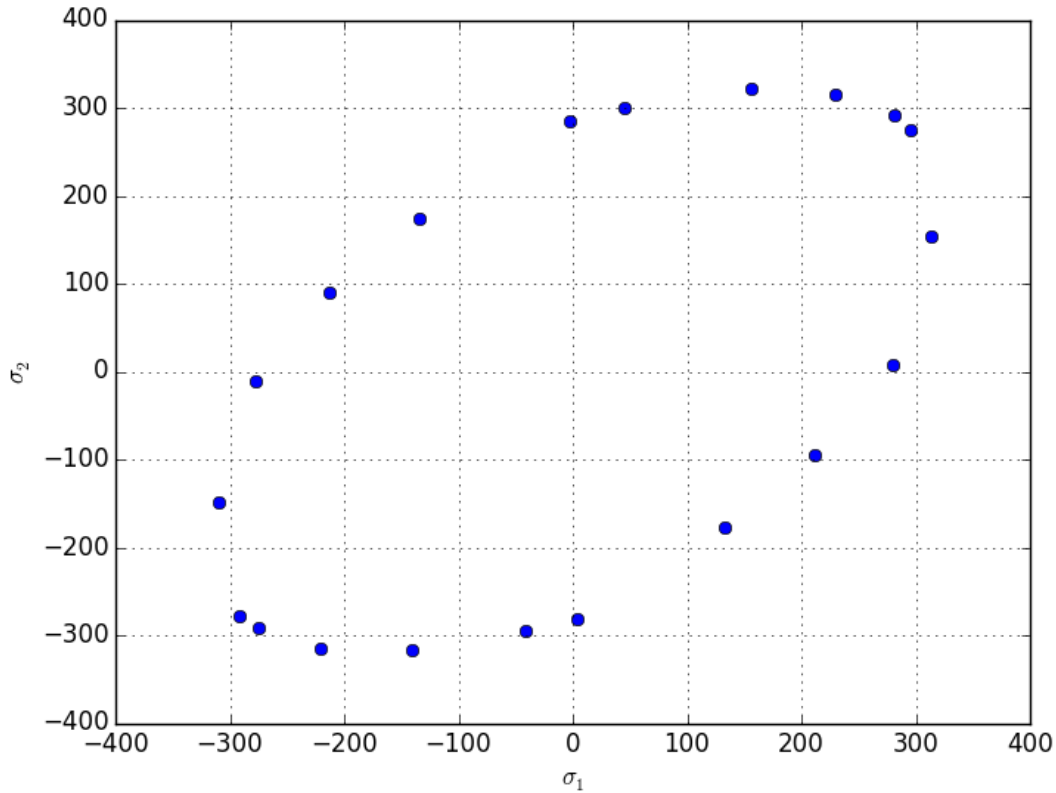


Figure 16: Plane stress state($\epsilon^p = 0.2$) generated by virtual tests

Compared with the plastic phenomenological power law model, HAH model are more tun-

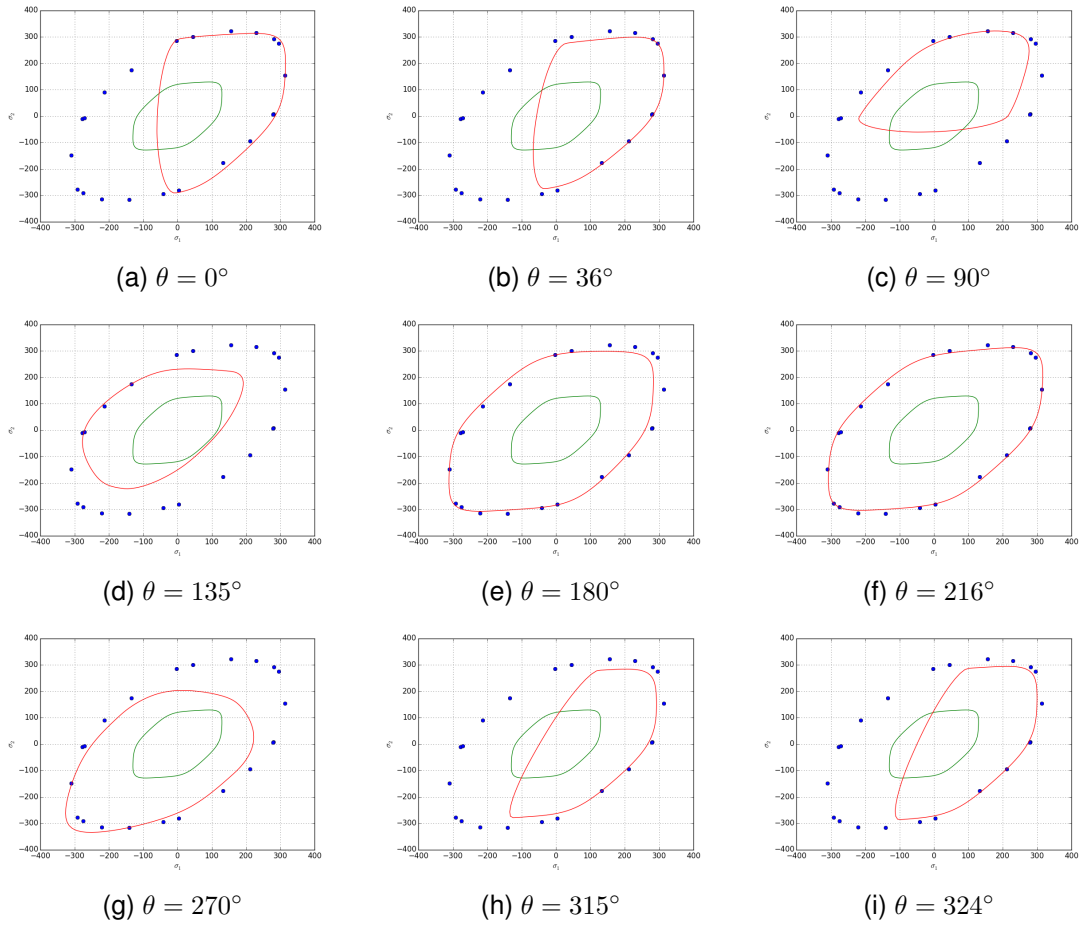


Figure 17: Virtual plane stress tests fit by Yld2000-2d+HAH model

	k_1	k_2	k_3	k_4	k_5	L	k_L	S	k_S	k
initial	250	10.0	0.10	0.9	10.0	1.0	0	1.35	100.0	30.0
$\theta = 0^\circ$	250	10.0	0.10	0.9	10.0	1.0	0	1.27	$-5.6e - 3$	31.94
$\theta = 36^\circ$	250	10.0	0.10	0.9	10.0	1.0	0	1.14	620.38	0.35
$\theta = 90^\circ$	250	10.0	0.10	0.9	10.0	1.0	0	1.23	26.35	292.12
$\theta = 135^\circ$	270.06	13.08	-0.12	0.90	9.77	1.0	0	1.35	100.65	21.25
$\theta = 180^\circ$	406.31	1.94	0.47	0.94	$3.5e - 8$	1.0	0	1.03	436.65	39.80
$\theta = 216^\circ$	534.98	$1.8e - 5$	0.58	0.93	4.62	1.0	0	1.15	3.75	13.19
$\theta = 270^\circ$	276.48	12.15	-0.04	0.90	9.87	1.0	0	1.35	100.22	21.08
$\theta = 315^\circ$	250	10.0	0.10	0.9	10.0	1.0	0	1.11	826.61	9.87
$\theta = 324^\circ$	250	10.0	0.10	0.9	10.0	1.0	0	6.01	0.05	9.05

Table 20: HAH model fit parameters

able, especially for the permanent softening and stress overshoot. By prestraining, plane stress tension($\theta = 36^\circ$) and uniaxial tension, the flow curve of 3-step virtual test is plot in Fig.(18). Due to the definition of phenomenological power law model, permanent softening and stress overshoot are not considered.

In the end, it is hard to say which plastic model is better as most models are phenomenological. Is it necessary to include so many parameters in the plastic model? Is there a simple model to explain every thing? The strain hardening problem waits for the fundamental breakthrough in physics.

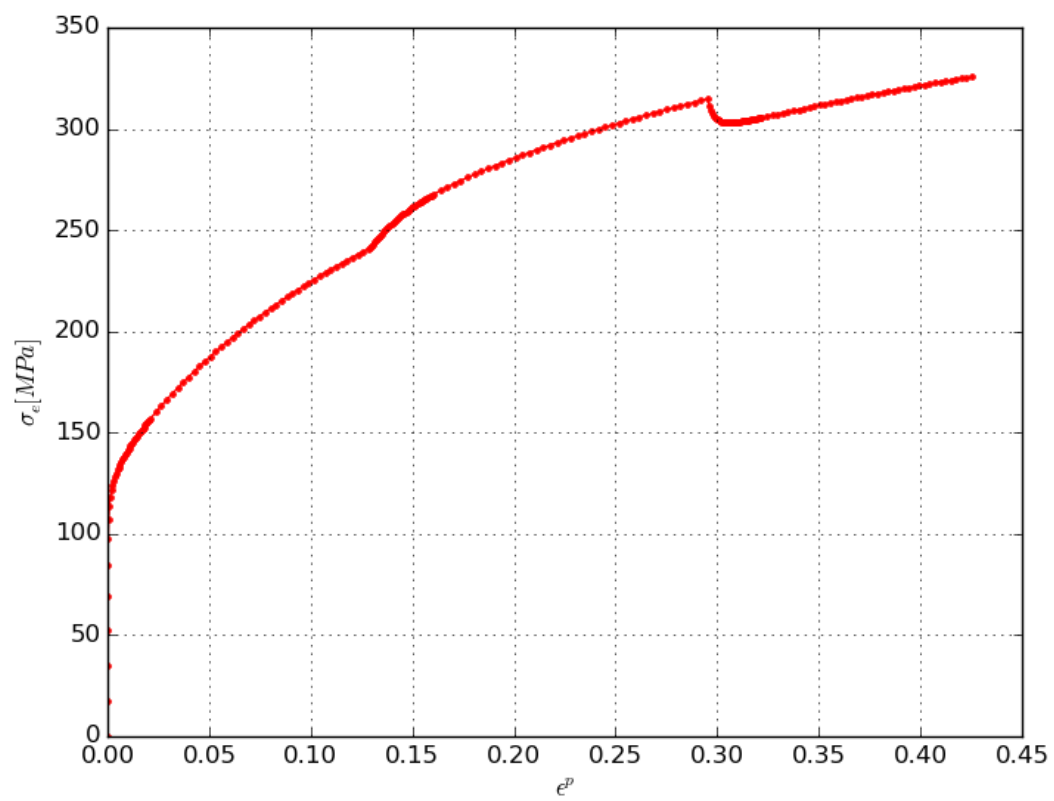


Figure 18: 3-step virtual test: prestrain, plane stress at 36° , uniaxial tension

4 Conclusion

In this paper, Armstrong-Frederick type back stress is added into the plastic phenomenological power-law model of DAMASK. An approach for slip phenomenological power-law material parameter calibration is proposed, which uses Taylor's M factor to give an initial guess for optimization. This approach is practiced by uniaxial tension-compression test and simple shear-reverse shear test. However, in general, the material parameter determination as an inverse problem is still open [5] [33]. The implicit constitutive relation in the plastic model controls the local material behavior, which largely decreases the unknown parameters so that the inverse material parameter determination can be achieved. Despite of the kinematic hardening on each slip system, homogeneous anisotropic hardening(HAH) model is also presented to describe the Bauschinger effect from a macroscopic view. HAH model uses more parameters than the kinematic hardening. But the material parameter determination of HAH model uses much less computational time than the that of kinematic hardening.

Apart from the problem of material parameter determination, strain hardening remains a difficult problem in classical physics. Most models considering dislocation density are phenomenological, which results a large number of parameters for a good description. Recently, an effective disorder temperature is introduced by James Langer [24] [23], which reduces the parameters to a small number from the view of non-equilibrium thermodynamics. It is expected that the description of dislocation can be simple and fundamental. Furthermore, considering the geometrically necessary dislocation, the strain gradient theory is developed to capture the size effect in the microscopic scale [12] [11]. Basically, it extends the deformation gradient to a higher order, which exhibits the local curvature. For implementation, the effective strain gradient is added into the plastic model or the strain gradient is added as another boundary condition for the equilibrium equation. A general theory of dislocation from geometric aspect is proposed in [22].

Plasticity which lies at the boundary of solid and fluid mechanics requires the knowledge of both fields as the study object is fluid-like solid. Therefore, it is expected that the simulation method for plasticity is no longer limited at solid mechanics (e.g. finite element method) but can also refer to fluid dynamics (e.g. lattice Boltzmann method [13]) and even statistical mechanics (e.g. phase field crystal model [10]).

References

- [1] F. Barlat, J. J. Gracio, M.-G. Lee, E. F. Rauch, and G. Vincze. An alternative to kinematic hardening in classical plasticity. *International Journal of Plasticity*, 27(9):1309–1327, 2011.
- [2] F. Barlat, J. Ha, J. J. Grácio, M.-G. Lee, E. F. Rauch, and G. Vincze. Extension of homogeneous anisotropic hardening model to cross-loading with latent effects. *International Journal of Plasticity*, 46:130–142, 2013.
- [3] F. Barlat, G. Vincze, J. Grácio, M.-G. Lee, E. Rauch, and C. Tomé. Enhancements of homogenous anisotropic hardening model and application to mild and dual-phase steels. *International Journal of Plasticity*, 58:201–218, 2014.
- [4] B. Berisha, P. Hora, A. Wahlen, and L. Tong. A combined isotropic-kinematic hardening model for the simulation of warm forming and subsequent loading at room temperature. *International Journal of Plasticity*, 26(1):126 – 140, 2010.
- [5] L. Borcea. Electrical impedance tomography. *Inverse problems*, 18(6):R99, 2002.
- [6] B. Clausen. Characterisation of polycrystal deformation by numerical modelling and neutron diffraction measurements. Technical report, Risoe National Lab., 1997.
- [7] D. Deka, D. S. Joseph, S. Ghosh, and M. J. Mills. Crystal plasticity modeling of deformation and creep in polycrystalline ti-6242. *Metallurgical and materials transactions A*, 37(5):1371–1388, 2006.
- [8] J. Den Toonder, J. Van Dommelen, and F. Baaijens. The relation between single crystal elasticity and the effective elastic behaviour of polycrystalline materials: theory, measurement and computation. *Modelling and Simulation in Materials Science and Engineering*, 7(6):909, 1999.
- [9] P. Eisenlohr, M. Diehl, R. A. Lebensohn, and F. Roters. A spectral method solution to crystal elasto-viscoplasticity at finite strains. *International Journal of Plasticity*, 46:37–53, 2013.
- [10] K. Elder and M. Grant. Modeling elastic and plastic deformations in nonequilibrium processing using phase field crystals. *Physical Review E*, 70(5):051605, 2004.
- [11] N. Fleck and J. Hutchinson. Strain gradient plasticity. *Advances in applied mechanics*, 33:296–361, 1997.
- [12] N. Fleck, G. Muller, M. Ashby, and J. Hutchinson. Strain gradient plasticity: theory and experiment. *Acta Metallurgica et Materialia*, 42(2):475–487, 1994.
- [13] A. N. Gorban and I. V. Karlin. Slow invariant manifolds for open systems. In *Invariant Manifolds for Physical and Chemical Kinetics*, pages 367–417. Springer, 2005.
- [14] M. E. Gurtin. A gradient theory of single-crystal viscoplasticity that accounts for geometrically necessary dislocations. *Journal of the Mechanics and Physics of Solids*, 50(1):5–32, 2002.

- [15] C.-S. Han, H. Gao, Y. Huang, and W. D. Nix. Mechanism-based strain gradient crystal plasticity—I. theory. *Journal of the Mechanics and Physics of Solids*, 53(5):1188–1203, 2005.
- [16] V. Hasija, S. Ghosh, M. J. Mills, and D. S. Joseph. Deformation and creep modeling in polycrystalline ti-6al alloys. *Acta Materialia*, 51(15):4533 – 4549, 2003.
- [17] Y. Huang, S. Qu, K. Hwang, M. Li, and H. Gao. A conventional theory of mechanism-based strain gradient plasticity. *International Journal of Plasticity*, 20(4):753–782, 2004.
- [18] M. Jirásek and Z. P. Bazant. *Inelastic analysis of structures*. John Wiley & Sons, 2002.
- [19] A. Koester, A. Ma, and A. Hartmaier. Atomistically informed crystal plasticity model for body-centered cubic iron. *Acta Materialia*, 60(9):3894 – 3901, 2012.
- [20] R. V. Kohn and A. McKenney. Numerical implementation of a variational method for electrical impedance tomography. *Inverse Problems*, 6(3):389, 1990.
- [21] M. Kraska, M. Doig, D. Tikhomirov, D. Raabe, and F. Roters. Virtual material testing for stamping simulations based on polycrystal plasticity. *Computational Materials Science*, 46(2):383–392, 2009.
- [22] E. Kröner. General continuum theory of dislocations and proper stresses. 1960.
- [23] J. Langer. Plastic flow of polycrystalline materials. In *APS Meeting Abstracts*, 2016.
- [24] J. Langer, E. Bouchbinder, and T. Lookman. Thermodynamic theory of dislocation-mediated plasticity. *Acta Materialia*, 58(10):3718–3732, 2010.
- [25] E. H. Lee. Elastic-plastic deformation at finite strains. *Journal of Applied Mechanics*, 36(1):1–6, 1969.
- [26] N. Manopulo, F. Barlat, and P. Hora. Isotropic to distortional hardening transition in metal plasticity. *International Journal of Solids and Structures*, 56:11–19, 2015.
- [27] P. R. Peters. *Yield functions taking into account anisotropic hardening effects for an improved virtual representation of deep drawing processes*. PhD thesis, Diss., Eidgenössische Technische Hochschule ETH Zürich, Nr. 22707, 2015.
- [28] C. Raemy, B. Berisha, and P. Hora. Determination of yield loci based on CP-Models for DC05. In *Advanced constitutive models in sheet metal forming: Proceedings of 8th Forming Technology Forum*, pages 135–138, Zürich, 2015. ETH-Zürich.
- [29] J. Rosenberg and H. Piehler. Calculation of the taylor factor and lattice rotations for bcc metals deforming by pencil glide. *Metallurgical Transactions*, 2(1):257–259, 1971.
- [30] F. Roters. Advanced material models for the crystal plasticity finite element method: development of a general cpfem framework. Technical report, Fachgruppe für Materialwissenschaft und Werkstofftechnik, 2011.
- [31] M. H. Sadd. *Elasticity: theory, applications, and numerics*. Academic Press, 2009.

- [32] A. Salem, S. Kalidindi, and S. Semiatin. Strain hardening due to deformation twinning in α -titanium: Constitutive relations and crystal-plasticity modeling. *Acta Materialia*, 53(12):3495 – 3502, 2005.
- [33] A. Tarantola. *Inverse problem theory and methods for model parameter estimation*. siam, 2005.
- [34] G. Taylor and U. Dehlinger. Strains in crystalline aggregate. In *Deformation and Flow of Solids/Verformung und Fliessen des Festkörpers*, pages 3–12. Springer, 1956.
- [35] C. Xie, S. Ghosh, and M. Groeber. Modeling cyclic deformation of hsla steels using crystal plasticity. *Journal of engineering materials and technology*, 126(4):339–352, 2004.
- [36] H. Zhang, M. Diehl, F. Roters, and D. Raabe. A virtual laboratory using high resolution crystal plasticity simulations to determine the initial yield surface for sheet metal forming operations. *International Journal of Plasticity*, 80:111–138, 2016.

Acknowledgments

The author thanks Dr. Franz Roters for the suggestion on the back stress implementation in DAMASK plastic phenomenological model. Thanks Bekim Berisha, Christian Raemy and Niko Manopulo for the fruitful discussion about kinematical hardening, DAMASK manipulation and HAH model. Also thanks Prof. Pavel Hora for allowing me to do the master thesis in the Institute of Virtual Manufacturing.

A Source code

DAMASK can be downloaded from <https://damask.mpie.de/>. Plastic phenopowerlaw model with back stress implemented can be download from https://github.com/puwe/DAMASK/blob/master/plastic_phenopowerlaw.f90. DAMASK has Python libs as interface for its core. Codes for material parameter calibration can be viewed in <https://github.com/puwe/DAMASK/blob/master/examples/SpectralMethod/ParamsFit.py>.